

1 **Bridging the gap between SOLA and Deterministic Linear** 2 **Inferences in the context of seismic tomography**

3 Adrian M. Mag¹, Christophe Zaroli², Paula Koelemeijer¹

¹ *Department of Earth Sciences, University of Oxford, Oxford, United Kingdom*

² *Institut Terre et Environnement de Strasbourg, Université de Strasbourg, EOST, CNRS, UMR 7063,*

5 rue Descartes, Strasbourg F-67084, France

4 Received date; in original form date

5 **SUMMARY**

6 Seismic tomography is routinely used to image the Earth's interior using seismic data. How-
7 ever, in practice, data limitations lead to discretised inversions or the use of regularisations,
8 which complicates tomographic model interpretations. In contrast, Backus-Gilbert inference
9 methods make it possible to infer properties of the true Earth, providing useful insights into
10 the internal structure of our planet. Two related branches of inference methods have been de-
11 veloped – the Subtractive Optimally Localized Averages (SOLA) method and Deterministic
12 Linear Inference (DLI) approaches – each with their own advantages and limitations. In this
13 contribution, we show how the two branches can be combined to derive a new framework
14 for inference, which we refer to as SOLA-DLI. SOLA-DLI retains the advantages of both
15 branches: it enables us to interpret results through the target kernels, rather than the imperfect
16 resolving kernels, while also using the resolving kernels to inform us on trade-offs between
17 physical parameters. We therefore highlight the importance and benefits of a more careful
18 consideration of the target kernels. This also allows us to build families of models, rather than
19 just constraining properties, using these inference methods. We illustrate the advantages of

20 SOLA-DLI using three case studies, assuming error-free data at present. In the first, we illus-
21 trate how properties such as different local averages and gradients can be obtained, includ-
22 ing associated bounds on these properties and resolution information. Our second case study
23 shows how resolution analysis and trade-offs between physical parameters can be analysed
24 using SOLA-DLI, even when no data values or errors are available. Using our final case study,
25 we demonstrate that SOLA-DLI can be utilised to obtain bounds on the coefficients of basis
26 function expansions, which leads to discretised models with specific advantages compared to
27 classical least-squares solutions. Future work will focus on including data errors in the same
28 framework. This publication is accompanied by a SOLA-DLI software package that allows the
29 interested reader to reproduce our results and to utilise the method for their own research.

30 **Key words:** Inverse theory, Seismology, Seismic tomography, Structure of the Earth, Surface
31 waves and free oscillations.

32 1 INTRODUCTION

33 Seismic tomography relies on mathematical inversions (Rawlinson et al. 2010; Nolet 2008) to
34 model Earth’s interior from collected data. Resulting tomography models highlight persistent fea-
35 tures, such as subducted plates, rising plumes, and large scale velocity anomalies, believed to
36 mirror real Earth characteristics (Ritsema & Lekić 2020). Improving these models often involves
37 the development of new models with different data or methods to enhance the resolution of certain
38 features or to reduce uncertainties. However, seismic inversions encounter a major challenge: data
39 scarcity. This leads to non-uniqueness in solutions (e.g. Tarantola 1987), which often is mitigated
40 using regularisation. Yet, such prior information might inadvertently impose unrealistic constraints
41 or introduce artefacts in the models (e.g. Nolet 2008; Zaroli et al. 2017). While incorporating such
42 new information is not inherently wrong, it must be accurate and well-understood to avoid misin-
43 terpretations of the resulting seismic tomography models.

44 In contrast, inference methods aim to constrain some specific properties of the unknown model.
45 In geophysics, these methods can be traced back to the seminal papers of Backus and Gilbert
46 (Backus & Gilbert 1967a,b, 1970), where they attempted to obtain the highest resolution local

47 averages of a continuous unknown model using just the data as constraints. The methodology in-
48 troduced in Backus & Gilbert (1970) has since been used in various branches of geophysics, e.g.
49 deconvolution (Oldenburg 1981), geomagnetism (Backus 1988a), seismology (Zaroli 2016). Fur-
50 thermore, this foundational work has inspired the development of two branches of linear inference
51 methods (See Fig. A1).

52 The first branch started with three contributions from Backus (Backus 1970a,b,c) where the
53 goal was to find a specific linear property of the unknown model, rather than just the highest res-
54 olution local average. Backus showed that data alone cannot provide any information on nearly
55 all linear properties, and introduced an additional prior constraint on the model space in the form
56 of a model norm bound (Backus 1970a). The use of prior model information (e.g. a norm bound)
57 is what distinguishes this branch, which we refer to as the DLI (Deterministic Linear Inference)
58 branch due to the deterministic nature of the norm bound prior information (as opposed to a prob-
59 abilistic prior information). Backus (1970b) and Backus (1970c) further investigated how to deal
60 with properties that cannot be naturally expressed on Hilbert spaces, and how to approach situa-
61 tions where we have bounds on the norm of a truncated expansion of the model rather than the
62 model itself. Parker (1977) re-derived the findings of Backus (1970a) in a modified framework,
63 defining a finite-dimensional “property–data” space separate from the infinite–dimensional model
64 space. This approach was then used to constrain the coefficients of a basis expansion for an un-
65 known model by applying data constraints along with a model norm bound that differed from the
66 one used by Backus (1970a). More recently, Al-Attar (2021) has placed the method of Backus
67 (1970a) and Parker (1977) in a more general mathematical framework.

68 The second branch has mainly been represented by the SOLA method (Subtractive Optimally
69 Localized Averages), developed by Pijpers & Thompson (1992, 1994), although similar methods
70 had previously been used in deconvolution theory (Oldenburg 1981). The SOLA branch was in-
71 troduced into the seismic tomography community by Zaroli (2016) and has received increasing
72 attention in the past decade (e.g. Zaroli et al. 2017; Lau & Romanowicz 2021; Latallerie et al.
73 2022; Amiri et al. 2023; Restelli et al. 2024). Fundamentally, SOLA resembles the method by
74 Backus (1970a), with the distinction that it lacks any prior model information such as the model

75 norm bound used in the DLI branch. In the absence of additional prior constraints, it yields only an
76 approximate local average – precisely defined by a resolving kernel R . Given an unknown model
77 \bar{m} , the Backus (1970a) method finds a set of possible values for $\int T\bar{m}$ (the desired property),
78 where T represents a predefined weight function, known as the target kernel. In contrast, SOLA
79 provides a single value, $\int R\bar{m}$ (the approximate property), under error-free conditions, where R
80 is similar to T . Consequently, results obtained with approaches from the DLI branch can be in-
81 terpreted in terms of the target kernels, whereas results from the SOLA branch are interpreted
82 through the resolving kernels (see Table A1).

83 The primary advantage of linear inference methods over inversions lies in their ability to pro-
84 vide detailed uncertainty and resolution analyses. However, this benefit comes at the cost of lin-
85 earity; these methods are only applicable to linear problems or weakly non-linear ones through
86 linearisation. While Snieder (1991) extended the method of Backus & Gilbert (1970) to address
87 weakly non-linear problems, the SOLA and DLI branches lack such generalisations. Furthermore,
88 compared to other linear methods, linear inference techniques are not ideal candidates for itera-
89 tive solvers, as they focus on extracting properties of the model rather than constructing models
90 (though, as we will show later, it is possible to build discretised models as well). In non-linear
91 problems, typically a non-linear method (such as Bayesian inversion) or an iterative solver is used
92 to arrive at a model that is considered relatively close to the true model. The employed methods
93 must have convergent properties, but they do not necessarily have the ability to provide resolu-
94 tion and uncertainty information. Linear inferences could then be used as a final step to provide
95 comprehensive uncertainty and resolution analysis.

96 We propose that the combination of the two methodological branches offers a more com-
97 prehensive base framework for geophysical inferences. By framing the interpretation in terms of
98 target kernels, as is implicitly done in the DLI branch, we ensure the results are easily and consis-
99 tently interpretable, which is particularly important for specific applications, such as determining
100 relationships between seismic velocities. If the interpretation is to be placed on the target kernels,
101 then we argue that more care should be taken when designing the target kernels. However, the
102 impact of target kernel selection has not been directly studied in the SOLA branch; simple target

103 kernels, such as boxcar and Gaussian functions, have typically been chosen for their ease of use
104 (e.g. Zaroli et al. 2017; Restelli et al. 2024). A more careful consideration of the target kernels not
105 only ensures that the advantage of easier interpretability is not lost, but it can also lead to tighter
106 property bounds, as we will demonstrate.

107 Although the DLI branch of methods does not require the explicit use of resolving kernels,
108 these kernels are central in the SOLA branch. We will demonstrate that, with a slight modifica-
109 tion of the SOLA approach, the resolving kernels can also be seen as an implicit component of
110 approaches in the DLI branch. Even within DLI methods, we can thus use these resolving kernels
111 to obtain additional insights into spatial trade-offs and contamination from other physical param-
112 eters. In addition, if the interpretation is placed on the target kernels, it is possible to use inference
113 methods to obtain discretised models, rather than just properties of models.

114 By combining the two branches, we obtain in essence a deterministic linear inference method,
115 similar to Al-Attar (2021), but with modified property bounds and a direct incorporation of resolv-
116 ing kernels (an idea stemming from SOLA) into the analysis. Therefore, this combination should
117 be regarded as a “SOLA-infused deterministic linear inference” method, which we will refer to as
118 “SOLA-DLI”.

119 In this contribution, we do not consider noise in the data. However, this does not mean that the
120 data are perfect. Even a noise-free dataset is not “perfect” if it lacks enough information to fully
121 constrain the model space to a single solution, i.e. it is incomplete. As Backus & Gilbert (1967a)
122 demonstrated, an infinite-dimensional model space requires an infinite number of independent
123 data to provide complete constraints. Both branches of linear inference methods discussed earlier
124 can address data noise and incompleteness, but they take fundamentally different approaches to
125 handling incompleteness. Approaches from the DLI branch integrate incompleteness errors into
126 the property bounds, while the SOLA branch captures these errors in the resolving kernels. No-
127 tably, the treatment of data noise varies even within each branch (e.g., Backus (1970a) outlines
128 two distinct approaches for handling them).

129 As the two methods we aim to combine differ fundamentally in how they address incomplete-
130 ness in the data, we focus in this work exclusively on errors arising from data incompleteness

rather than data noise. As a result, the framework we present is not immediately ready for most real-world applications, but it forms a foundation for future developments where data noise will be incorporated. In the mean time, the theory already has potential practical applications even without data noise considerations. For example, in design optimisation problems, where data have yet to be measured, it is the “geometry of the dataset” that drives the optimisation problem. This is exactly an element that can be addressed with the theory presented here.

The remainder of this paper is organised as follows: Section 2 firstly explores the relationship between the DLI and SOLA branches, before combining them into the joint SOLA-DLI framework. In addition, we discuss the use of target and resolving kernels in SOLA-DLI, specifically, showing how the choice of target kernels influences the types of properties that can be constrained and how some may be better constrained than others. It further develops the theoretical framework for cases involving multiple physical parameters, explaining the roles and interpretations of resolving and contaminant kernels within this context. Additionally, it demonstrates how families of models can be derived using DLI-based inference methods. Section 3 presents three practical examples with synthetic, noise-free data to illustrate the theoretical concepts introduced in Section 2. Finally, Sections 4 and 5 provide a discussion and conclusion, respectively. Appendix A provides a general perspective on inference methods, while appendices B,C,D provide supplementary mathematical derivations that offer additional detail to support Section 2.

2 THEORY

In this section we will mathematically describe the link between the two branches of linear inferences, taking the DLI branch as starting point and subsequently introducing elements from the SOLA branch to establish the SOLA-DLI framework. We also examine how the choice of target kernels influences the inference outcomes and discuss key considerations necessary for ensuring the correct interpretation of results. Additionally, we demonstrate how resolving kernels can be employed to analyse trade-offs between physical parameters and how the model norm bound can serve to estimate these trade-offs, offering a potential alternative to the 3D noise method employed so far (Masters & Gubbins 2003; Restelli et al. 2024). Finally, we evaluate the strengths and lim-

158 itations of linear inference methods for deriving discretised models, highlighting why “models”
 159 obtained with SOLA should strictly speaking be considered proxies to a model, rather than an
 160 actual model.

161 Throughout the paper, we will adopt a modern mathematical notation similar to Al-Attar
 162 (2021), which is applicable to both Banach and Hilbert spaces. This operator-based formalism
 163 is particularly well-suited for comparing and combining the SOLA and DLI methods, as it more
 164 readily clarifies the connections between these approaches.

165 2.1 Combining the DLI and SOLA branches into SOLA-DLI

166 2.1.1 Deterministic Linear Inferences

167 Let d be some error-free data, m a model, and G a linear forward operator. We can express the
 168 model-data relationship as follows:

$$G(m) = d. \quad (1)$$

169 We refer to such model-data relationships as “deterministic data constraints”, assuming the data
 170 are known exactly (no data noise). The model belongs to a model space \mathcal{M} , while the data reside
 171 in a data space \mathcal{D} . In inversions, we aim to find the model solution from the data by inverting
 172 the forward relation (Equation 1). However, in most cases, the forward relation cannot be inverted
 173 due to insufficient or inadequate data. For continuous models, this scenario can result in either
 174 no solutions or infinitely many solutions (Backus & Gilbert 1967b). In the absence of data noise,
 175 no solutions occur only when the data lie outside the range of the forward operator, making them
 176 incompatible with the physical laws governing the system. Typically, in such situations, we would
 177 employ a different forward relation. Throughout this paper, we will assume that the data are com-
 178 patible with the forward relation, leading to an infinite set of solutions, denoted by S (see Fig. 1a).
 179 Inversions can then be conducted by imposing constraints (regularisations) on the model space \mathcal{M}
 180 until a single model, \tilde{m} , is “selected”. For instance, one might choose the model with the smallest
 181 average gradient (the flattest model), or with the smallest norm. However, if the implicit assump-

182 tions of the chosen regularisation are incorrect, the resulting model may not accurately represent
183 reality.

184 We often seek specific properties of the true model \bar{m} rather than the entire model itself. These
185 properties, for example the average structure over some volume within the Earth or the depths of
186 discontinuities, belong to a distinct space known as the property space \mathcal{P} , following the work of
187 Al-Attar (2021). Therefore, we can define a different (inference) problem as:

Given that:

$$G(\bar{m}) = d \quad (2)$$

Find:

$$\mathcal{T}(\bar{m}) = \bar{p} \quad (3)$$

188 where \mathcal{T} (the property mapping) is a linear relation that extracts a property of any model, and
189 $\bar{p} \in \mathcal{P}$ represents the value extracted by \mathcal{T} when applied to the true model \bar{m} . It can be shown
190 that in most practical situations, the desired property \bar{p} can take any value given a finite number
191 of deterministic data constraints (Al-Attar 2021; Backus 1970a). In other words, given the data
192 constraints, \bar{p} may take any value from the property space \mathcal{P} (see Fig. 1a), leaving us unable to
193 definitively determine the property of the true model \bar{m} . Backus (1970a) demonstrated that this
194 issue can be overcome by introducing a norm bound M in the model space:

$$\|m\|_{\mathcal{M}} \leq M. \quad (4)$$

195 This constraint on the model space differs from constraints typically imposed during regularisation
196 because it does not aim to isolate a single model. Instead, the model norm bound restricts solutions
197 to a bounded subset of \mathcal{M} . If the set of models satisfying the norm bound is denoted by U_M
198 (Equation 4), then the set of solutions respecting both the norm bound and the data constraint
199 is $U_M \cap S$, which is a bounded subset (Al-Attar 2021). Al-Attar (2021) further showed that this
200 constraint results in the true property \bar{p} being confined within a bounded subset $P \subset \mathcal{P}$, provided
201 that the norm of the true model is less than the chosen norm bound (see Fig. 1b for a visual
202 representation of these concepts). Note that the subset P is not a sharp bound on the values of the

203 true property, meaning that $\mathcal{T}(U_M \cap S) \subseteq P$ (theoretically, better approximations are possible).
 204 Without additional prior information, all properties in P are equally likely to represent the true
 205 property \bar{p} .

206 If the model space \mathcal{M} , data space \mathcal{D} , and property space P are Hilbert spaces, and the forward
 207 and property mappings G, \mathcal{T} are continuous linear mappings with G being surjective, then the
 208 solution to Equation 3 with data and model norm bound constraints (Equations 1 and 4) is given
 209 by (Al-Attar 2021):

$$\bar{p} \in \{p \in \mathcal{P} \mid \langle \mathcal{H}^{-1}(p - \tilde{p}), p - \tilde{p} \rangle \leq M^2 - \|\tilde{m}\|_{\mathcal{M}}^2\} \quad (5)$$

210 where \tilde{m} is the least norm solution to the data constraint (Equation 1), and $\tilde{p} = \mathcal{T}(\tilde{m})$ is the desired
 211 property of the least norm solution. This result implies that the true property \bar{p} lies within a hyper-
 212 ellipsoid defined by the inequality in Equation 5. The shape of this hyperellipsoid is determined
 213 by the operator \mathcal{H} , which is given by Al-Attar (2021):

$$\mathcal{H} = \mathcal{T}\mathcal{T}^* - \mathcal{T}G^*(GG^*)^{-1}GT^*. \quad (6)$$

214 It can further be shown that GG^* is invertible (Al-Attar 2021), if the model and data space are
 215 Hilbert spaces, and if G is a continuous linear and surjective mapping (we provide proof of its
 216 surjectivity in Appendix B).

217 2.1.2 Considerations on the model norm bound

218 The true model properties lie within the property bounds only if the norm of the true model is
 219 smaller than or equal to the norm bound. Therefore, it is crucial to choose a conservative norm
 220 bound in order to minimise the risk of inferring incorrect information about the true model. Typi-
 221 cally, we select the norm bound to be greater than the norm of the least norm solution (which we
 222 will simply refer to as the least norm from here on).

223 Higher norm bounds result in larger property bounds, which in turn reduces the inference
 224 power. If it is not possible to justify a sufficiently small norm bound that results in meaningful
 225 property bounds, then a least norm regularisation should not be used either. At first glance, the
 226 norm bound might appear to be a stringent constraint that is difficult to justify physically. In con-

227 trast, least norm regularisation, commonly used in inversion problems, simply assumes that “the
228 true model should have a small norm”. However, such regularisation essentially selects a single
229 model, which is actually more stringent than the inequality constraint used in inference methods.

230 Deriving a norm bound directly from physical arguments is often challenging, but it is possible
231 in specific cases. For example, when modeling the Earth’s magnetic field using spherical harmonic
232 coefficients, physical constraints like power dissipation can provide a norm bound. In seismology,
233 point-wise upper bounds on properties are often more accessible. From these bounds, a model
234 norm bound can be derived by constructing a piecewise function $\bar{m}(x) \leq b(x)$, leading to:

$$\int_{\Omega} \bar{m}^2 d\Omega \leq \int_{\Omega} b^2 d\Omega = M^2.$$

235 While this approach transforms point-wise bounds into an L_2 norm bound, it often overesti-
236 mates the bounds, resulting in overly large property bounds. A more precise alternative would be
237 the supremum norm:

$$\|m\|_{\infty} = \sup_{x \in \Omega} |m(x)|.$$

238 Alternatively, bounds based on model regularity (e.g., smoothness constraints) may be adopted, but
239 they involve Sobolev spaces that account for derivatives. Although such approaches are more rig-
240 orous, they are mathematically complex and not fully developed, as discussed in Al-Attar (2021).
241 Here, we use the L_2 norm for simplicity as the exploration of alternative norms is beyond the scope
242 of our work, but we acknowledge that other norms may be better suited.

243 2.1.3 *SOLA and resolving kernels*

244 We can specificise the DLI inference problem to obtain the theory of Backus (1970a) by assuming
245 the following form for the data and property mapping:

$$[G(m)]_i = \langle K_i, m \rangle_{\mathcal{M}} \quad (7)$$

$$[\mathcal{T}(m)]_k = \langle T^{(k)}, m \rangle_{\mathcal{M}}, \quad (8)$$

246 where $\langle \cdot, \cdot \rangle_{\mathcal{M}}$ denotes the model space inner product, $K_i \in \mathcal{M}$ are data sensitivity kernels, and
247 $T^{(k)} \in \mathcal{M}$ are target kernels. Then Equations 5 and 6 correspond to the solution of Backus (1970a,

Equation 4). We note that only the target kernels $T^{(k)}$ and sensitivity kernels K_i appear in this formulation; resolving kernels are neither required nor used.

Resolving kernels do play a role in SOLA-type linear inferences, where the problem described by Equations 2 and 3 is “solved” without incorporating prior information on the model norm bound. However, the SOLA framework usually assumes an even more specific form for the data and property mapping than that shown in Equations 7 and 8, namely:

$$[G(m)]_i = \int_{\Omega} K_i m d\Omega \quad (9)$$

$$[\mathcal{T}(m)]_k = \int_{\Omega} T^{(k)} m d\Omega, \quad (10)$$

which corresponds to choosing the model space inner product to be

$$\langle f, g \rangle_{\mathcal{M}} = \int_{\Omega} f g d\Omega.$$

and the model space to be some corresponding function space, such as $L^2[\Omega]$, where Ω is some spatial domain. This choice of inner product, which is normally implicitly assumed in SOLA-type inference problems, has implications for the norm bound and its effectiveness. In particular, using this inner product leads to the following norm:

$$\|m\|_{\mathcal{M}} = \int_{\Omega} f^2 d\Omega. \quad (11)$$

The goal of SOLA is to find some real weights $x_i^{(k)}$ such that (Zaroli 2019):

$$\int_{\Omega} T^{(k)} \bar{m} d\Omega \approx \int_{\Omega} \sum_i^{N_d} x_i^{(k)} K_i \bar{m} d\Omega \quad (12)$$

where N_d is the number of sensitivity kernels and the dimension of the data space $\mathcal{D} = \mathbb{R}^{N_d}$. The resolving kernels are then defined to be:

$$R^{(k)} = \sum_i^{N_d} x_i^{(k)} K_i \quad (13)$$

The resulting SOLA solution is given by:

$$\operatorname{argmin}_{x_i^{(k)}} \left[\int_{\Omega} (T^{(k)} - \sum_i^{N_d} x_i^{(k)} K_i)^2 d\Omega \right] \quad (14)$$

$$\text{s.t. } \int_{\Omega} R^{(k)} d\Omega = 1 \quad (15)$$

263 This constrained optimisation problem will provide the weights that will produce unimodular re-
 264 solving kernels similar to the target kernels. Subsequently, the true properties can be approximated
 265 by:

$$[\mathcal{T}(\bar{m})]_k \approx [\mathcal{R}(\bar{m})]_k = \int_{\Omega} R^{(k)} \bar{m} d\Omega. \quad (16)$$

266 If we drop the unimodularity condition (Equation 15), then it can be shown (Appendix C) that the
 267 solution to the optimisation problem in Equation 14 is the same as the solution to:

$$\int_{\Omega} T^{(k)} K_j d\Omega - \sum_i^{N_d} \left(\int_{\Omega} K_j K_i d\Omega \right) x_i^{(k)} = 0. \quad (17)$$

268 It is obvious from Equation 9-10 that:

$$\int_{\Omega} T^{(k)} K_j d\Omega = [\mathcal{T}G^*]_{kj} \quad (18)$$

$$\int_{\Omega} K_j K_i d\Omega = [GG^*]_{ji} \quad (19)$$

269 If we further define $X_{ki} = x_i^{(k)}$, then we find:

$$X = \mathcal{T}G^*(GG^*)^{-1}. \quad (20)$$

270 Therefore, $X : \mathcal{D} \rightarrow \mathcal{P}$ is a linear mapping that maps from the data space to the property space. In
 271 the absence of the unimodularity condition (Equation 15), $X(d)$ will be the solution in the SOLA
 272 framework, obtained here without the need for a model norm bound. It is also obvious that:

$$\mathcal{R} = XG = \mathcal{T}G^*(GG^*)^{-1}G \quad (21)$$

273 This is the same operator that can be recognised within the definition of \mathcal{H} in Equation 6. This
 274 shows that resolving kernels are implicitly present in the solution of the norm-bound (DLI) branch
 275 of inference methods. In fact, we have the relation:

$$\mathcal{H} = (\mathcal{T} - \mathcal{R})(\mathcal{T} - \mathcal{R})^*, \quad (22)$$

276 which shows that the matrix \mathcal{H} encodes the difference between resolving kernels and target kernels.
 277 This difference arises due to data incompleteness and can only be quantified in the property space
 278 when norm prior bounds on the model space are incorporated.

279 *2.1.4 The combined SOLA-DLI framework*

280 After establishing the link between the DLI and SOLA branches, combining the two primarily
 281 involves a practical step. This step entails calculating both the property bounds (using Equation 5)
 282 and the resolving kernels (using Equation 20), and interpreting the final result using both.

283 In addition, we also introduce a small modification to Equation 5. It can be shown that if
 284 Equation 5 holds, the following is also true (see Appendix D3):

$$\tilde{p}^{(k)} \in [\tilde{p}^{(k)} - \epsilon^{(k)}, \tilde{p}^{(k)} + \epsilon^{(k)}], \quad (23)$$

285 where

$$\epsilon^{(k)} = \sqrt{(M^2 - \|\tilde{m}\|_{\mathcal{M}}^2) \mathcal{H}_{kk}}. \quad (24)$$

$$\tilde{p} = \mathcal{T}(\tilde{m}) = \mathcal{R}(\tilde{m}) \quad (25)$$

286 Equation 23 represents a hyperparallelepiped in \mathcal{P} that encloses the hyperellipsoid defined by
 287 Equation 5. This provides more conservative error bounds. The rationale for this modification is
 288 twofold. Firstly, Equation (5) requires the computation of the full matrix \mathcal{H} and solving a system
 289 of linear equations involving \mathcal{H}^{-1} . In contrast, Equation 23 only needs the diagonal terms of
 290 \mathcal{H} , thus decreasing the computational cost significantly. Secondly, while Equation 5 incorporates
 291 information about the trade-offs between error bounds of different properties, this information is
 292 often difficult to visualise and interpret in practice. Conversely, Equation 23 can be easily plotted
 293 (visual explanation as to why this is the case is given in Fig. A2), making it more practical for
 294 applications.

295 Historically, the DLI branch has been applied primarily to models involving a single phys-
 296 ical parameter, whereas the SOLA approach has also been employed for cases where the data
 297 depend on multiple physical parameters simultaneously (e.g. Masters & Gubbins 2003; Restelli
 298 et al. 2024). This historical distinction may partly explain why resolving kernels have traditionally
 299 not been used in the DLI branch, as their utility becomes more significant when dealing with mul-
 300 tiple physical parameters. We will further explore the increased significance of resolving kernels
 301 in the context of multiple physical parameters in Section 2.3, where we discuss the concept of

contaminant kernels. However, given the importance of the target kernels, we first revisit these in the next section.

2.2 Choice of Target Kernels

Different information about the unknown model can be extracted by choosing appropriate target kernels, which need to be carefully designed if we interpret the results through them. To illustrate this, we introduce a simplified setup, where we assume the model to be a triplet of piece-wise continuous and bounded functions $m = (m^1, m^2, m^3)$ defined on the interval $[0, 1]$. This leads to a 1D inference problem, however, the results can be easily generalised. The true model is assumed to be known and is plotted in Fig. 2. This model is arbitrary and has no physical significance.

2.2.1 Local Average Targets

Previous studies have primarily used the box car function as a target kernel for its simplicity and ease of interpretation - it gives a uniform local average (Restelli et al. 2024; Masters & Gubbins 2003). However, many other types of target kernels could be used to obtain local averages. Here, we introduce three different averaging target kernels:

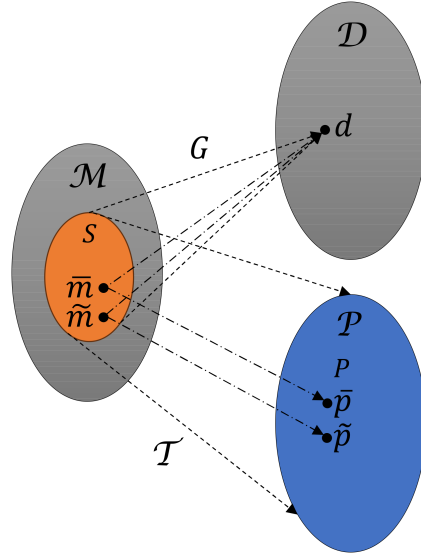
Uniform Local Average (for reference):

$$T_U^{(k)}(r) := \begin{cases} C & r \in V_k \\ 0 & \text{else} \end{cases} \quad (26)$$

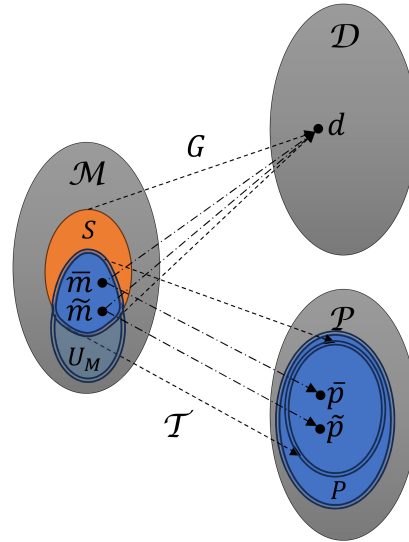
316

Gaussian Local Average:

$$T_G^{(k)}(r) := C \exp \left[-\frac{\|r - r^k\|_2^2}{2\sigma^2} \right] \quad r \in \Omega \quad (27)$$



(a) No norm bound applied on the model space.



(b) With a norm bound applied on the model space.

Figure 1. Schematic of general linear inference problems, illustrating the effect of bounding the model space (see Table A1 for symbol definitions). Sets with thin lines for margins represent unbounded sets, while sets with double line margins represent bounded sets. The true model is denoted by \bar{m} and the least norm model solution is denoted by \tilde{m} . a) When no bounds are imposed, the property of a model that respects the data constraint may take any value in the property space, which is an unbounded set (see Al-Attar 2021, Theorem 2.2). In other words, $\mathcal{T}(S) = P = \mathcal{P}$. b) Applying the norm bound on the model space leads to the intersection between S and U_M to be bounded, which gets mapped under \mathcal{T} to a bounded subset of \mathcal{P} . We thus have the following relation: $\mathcal{T}(U_M \cap S) \subseteq P \subset \mathcal{P}$.

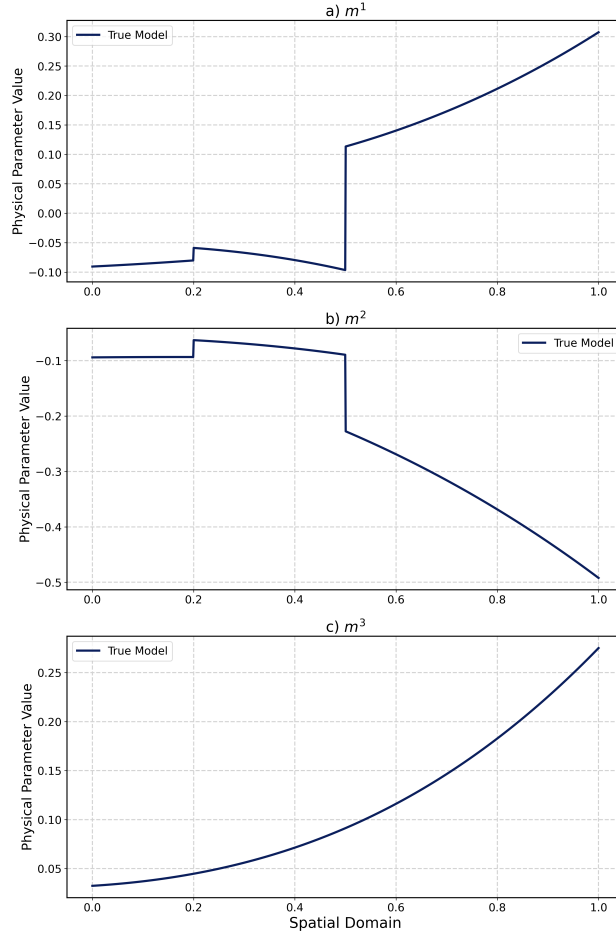


Figure 2. An arbitrary synthetic “true model”. m^j denotes the physical parameters of the model.

317

Bump Function Average:

$$T_B^{(k)}(r) := \begin{cases} C \exp \left[\frac{w^2}{2(r-r^{(k)})^2 - w^2} \right] & r \in V_k \\ 0 & \text{else} \end{cases} \quad (28)$$

318 where

$$V_k = \left[r^{(k)} - \frac{w}{2}, r^{(k)} + \frac{w}{2} \right] \quad (29)$$

319 is the compact support of the boxcar and bump function with width w , σ is the standard deviation of the Gaussian, and C is in each case an appropriate normalisation constant that ensures the
 320 unimodularity of each target kernel. Examples of these averaging kernels are plotted in Fig. 3. Us-
 321 ing these target kernels we can define, for example, the following property mappings for physical
 322

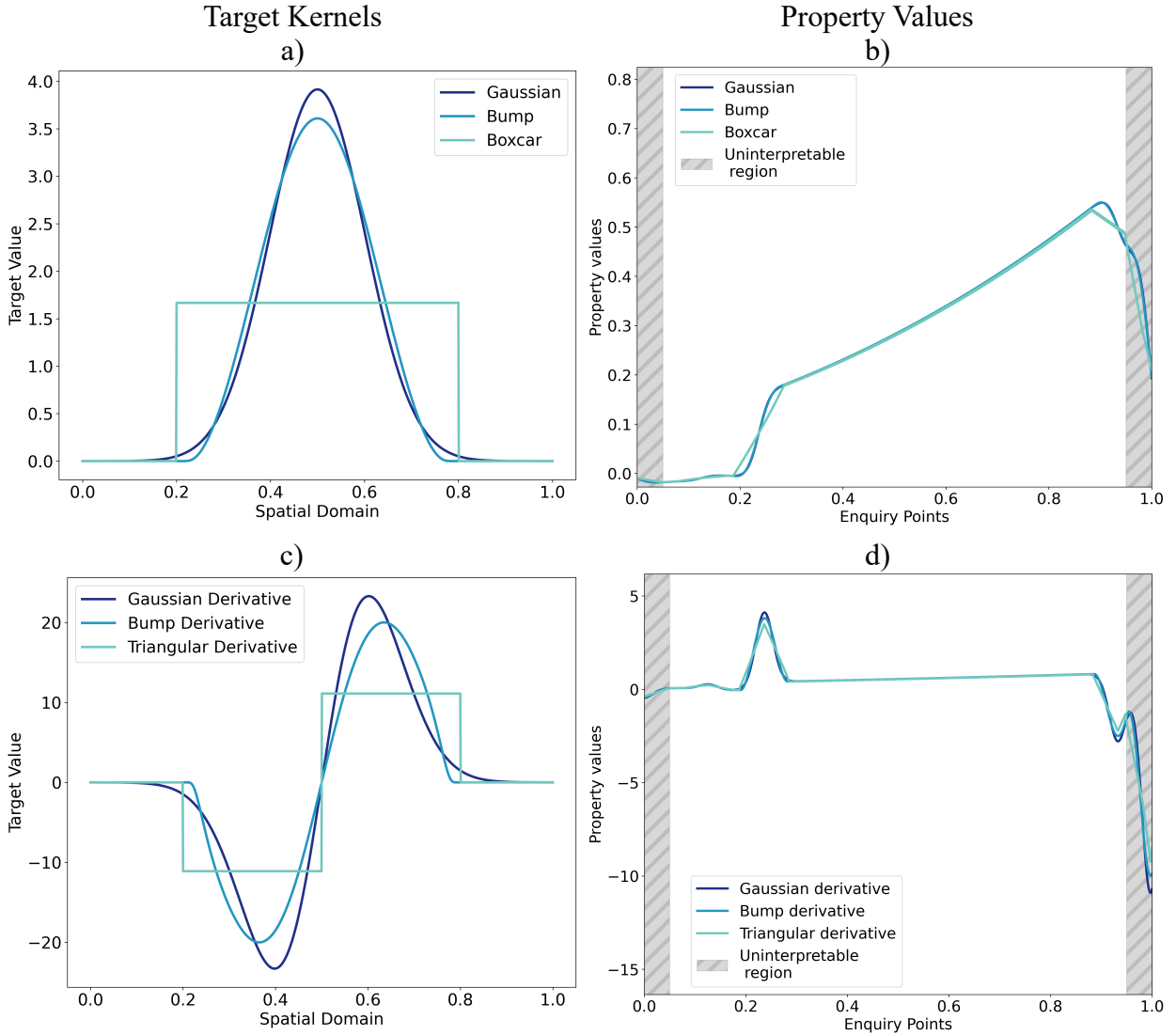


Figure 3. Examples of averaging (a) and gradient (c) target kernels and corresponding properties of model parameter m^1 (b and d) obtained using these target kernels. First column: averaging and gradient target kernels with width 0.6. Second column: property values as a function of 1000 enquiry points for different local averages and gradients of the true model using target kernels with width 0.1. The grey hatched regions represent parts of the domain where the target kernels are clipped (half-width of the target kernels). The target kernels for physical parameters m^2, m^3 are 0 since we are not interested in these parameters.

parameter m^1 :

$$\bar{p}_{U/G/B}^{1,(k)} = \mathcal{T}_{U/G/B}(m) = \int_0^1 T_{U/G/B}^{1,(k)}(r) m^1(r) dr. \quad (30)$$

The property vector extracted by each such property mapping (uniform/Gaussian/bump) is a vector of local averages centered at a set of points $\{r^{(k)}\}$ that we call “enquiry points”. In Fig. 3 we also plot the property vectors $\bar{p}_{U/G/B}^{1,(k)}$ for 1000 evenly spaced enquiry points (right column). The grey

327 hatched regions are parts of the domain where the target kernels $T_{U/G/B}^{1,(k)}$ are clipped and therefore
 328 their associated results uninterpretable.

329 Each of these target kernels has advantages and disadvantages. The boxcar function (Restelli
 330 et al. 2024) is simple and has compact support, providing a clear interpretation of the resolution of
 331 these kernels. However, most sensitivity kernels used in seismology are smooth, typically giving
 332 rise to poor resolving kernels that do not resemble boxcar functions. Consequently, the property
 333 error bounds are large.

334 Gaussian targets are often better reconstructed and thus lead to better constrained property val-
 335 ues. They are, however, not defined on a compact domain and restricting a Gaussian to a compact
 336 domain leads to clipping. A clipped Gaussian is no longer a Gaussian, and different centering of
 337 the Gaussian leads to different clipping and therefore a “non-uniform” interpretation of the prop-
 338 erty values. If most of the Gaussian is located well within the bounds of the model domain, then
 339 the errors introduced by clipping can be negligible, but not readily quantifiable. For such target
 340 kernels we define a “width” that contains some large and arbitrary percentage of the function’s
 341 weight (such as 90%) and pretend as if the entire weight of the function is concentrated in this
 342 region.

343 Bump functions are both smooth and defined on a compact support, therefore offering some of
 344 the advantages of both boxcars and Gaussian targets. The one shown here is just one example of a
 345 family of functions with similar characteristics.

346 2.2.2 *Local Gradient Targets*

347 If we want to obtain some local estimate of the gradient of a 1D physical parameter such as:

$$\bar{p}^{l,(k)} = \int_0^1 T^{l,(k)} \frac{dm^l}{dr} dr \quad (31)$$

348 we can use integration by parts to obtain:

$$\bar{p}^{l,(k)} = - \int_0^1 \frac{dT^{l,(k)}}{dr} m^l dr + [T^{l,(k)} m^l]_0^1. \quad (32)$$

349 For target kernels $T^{l,(k)}$ with compact support Equation 32 will reduce to:

$$\bar{p}^{l,(k)} = - \int_0^1 \frac{dT^{l,(k)}}{dr} m^l dr \quad (33)$$

350 in the interval where the target kernels are not clipped. For any other target kernel, the second term
 351 will not necessarily be 0. However, it will be very close to zero if the target kernel is centered well
 352 within the bounds of the domain. Therefore, we can use Equation 33 to define new target kernels
 353 that extract local gradients of the true model.

354 In the bottom row of Fig. 3 we plot the derivative of a Gaussian, Bump, and a Triangular
 355 function. The derivative of a Boxcar gives a sum of Dirac delta distributions. These cannot be used
 356 in our framework as they do not belong to a useful Hilbert space. Instead, we have opted for the
 357 derivative of a triangular function, which yields a Haar function. It is clear from Fig. 3d that the
 358 true property values obtained using the different gradient target kernels pick out the discontinuities
 359 of the true model.

360 The idea of using different target kernels to extract different types of information about the
 361 unknown model has been applied previously in helioseismology by Pijpers & Thompson (1994).
 362 They used Gaussian target kernels for extracting average information, and derivatives of the Gaus-
 363 sian to extract first and higher order derivatives of the model. However, as far as we are aware,
 364 this approach has not yet been used in seismic tomography. More importantly, the work of Pi-
 365 jpers & Thompson (1994) regard this approach as an inversion, whereas we believe it should be
 366 considered as an inference problem instead. While Lau & Romanowicz (2021) investigated dis-
 367 continuities inside the Earth using a SOLA approach, they used scalar value targets for the change
 368 across discontinuity and half-Gaussian target kernels to determine volumetric trade-offs.

369 2.3 Resolving and Contaminant Kernels

370 In seismology, we often analyse data that depend on multiple physical parameters, e.g. compres-
 371 sional wave speed (v_p), shear wave speed (v_s), and density (ρ). In general, this dependence can be
 372 expressed as:

$$[G(m)]_i = \sum_j^{N_m} \int_{\Omega} K_i^j m^j d\Omega, \quad (34)$$

where N_m represents the number of physical parameters. The property mapping can then be described by:

$$[\mathcal{T}(m)]_k = \sum_j^{N_m} \int_{\Omega} T^{j,(k)} m^j d\Omega. \quad (35)$$

If we consider each physical parameter as residing in its own Hilbert space ($m^j \in \mathcal{M}_j$), the model space can be defined as the direct sum of these individual spaces. Consequently, a model is represented as a tuple:

$$m = (m^1, m^2, \dots, m^{N_m}). \quad (36)$$

Furthermore, a norm bound for this composite model space can be derived from independent norm bounds applied to each physical parameter. This is given by:

$$\|m\|_{\mathcal{M}} = \sum_j^{N_m} \|m^j\|_{\mathcal{M}_j}. \quad (37)$$

The solution for the property bounds is then provided by Equation 5, while the corresponding resolving kernels are expressed as:

$$R^{j,(k)} = \sum_i^{N_d} x_i^{(k)} K_i^j. \quad (38)$$

It is important to note that every target kernel has an associated resolving kernel. When we are interested in a specific property of the l -th physical parameter, we typically set all the target kernels associated with other physical parameters to zero. Ideally, their associated resolving kernels would then also be zero or close to zero. However, in practice, these resolving kernels are rarely zero. This discrepancy increases the property bounds, making it more difficult to constrain the desired property. This issue effectively highlights the trade-offs that exist between physical parameters, thus providing useful information when interpreting the results. Notably, if a property of the l -th parameter strongly trades off with the l' -th parameter, this will be visible in the l' -th resolving kernel.

Any resolving kernel that is non-zero when it should ideally be zero is referred to as a contaminant kernel. Lau & Romanowicz (2021) used such contaminant kernels to quantify errors arising from trade-offs within a SOLA context. By using the model norm bound in our SOLA-DLI ap-

394 proach, we effectively and automatically account for these trade-offs, as they are integrated into
 395 the property bounds.

396 2.4 Obtaining Discretised Models through Target Kernels

397 One perceivable downside of linear inferences, such as SOLA-DLI, is the seeming impossibility of
 398 obtaining models that cover the full spatial domain (Valentine & Sambridge 2023). We illustrate
 399 here how SOLA-DLI can in fact be used to obtain discretised models by choosing appropriate
 400 target kernels, and discuss some advantages compared to simpler, classic inversions.

401 Consider a model $m \in \mathcal{M}$ related to some data $d \in \mathcal{D}$ by:

$$d_i = [G(m)]_i = \langle K_i, m \rangle_{\mathcal{M}}. \quad (39)$$

402 A common method to remove non-uniqueness, besides regularisation, is discretisation. Typically,
 403 a set of orthonormal basis functions $\{B_l\} \in \mathcal{M}$ is chosen and any model in \mathcal{M} is projected on the
 404 subspace formed by the span of this set, leading to a parallel m^{\parallel} and perpendicular m^{\perp} component
 405 of the model (i.e. m^{\parallel} is the component that can be expressed with $\{B_l\}$ and m^{\perp} is the residual
 406 term):

$$m = m^{\parallel} + m^{\perp} \quad (40)$$

$$m^{\parallel} = \sum_l p_l B_l \rightarrow \text{projection} \quad (41)$$

$$m^{\perp} = m - m^{\parallel} \quad (42)$$

407 where p_l are the coefficients given by the projection of m onto the basis functions:

$$p_l = \langle B_l, m \rangle_{\mathcal{M}} \quad (43)$$

408 We can then reformulate the initial inverse problem as:

$$\begin{aligned} &\text{Find } \{p_l\} \text{ s.t.} \\ &G\left(\sum_l p_l B_l\right) = d_i - G(\bar{m}^{\perp}) \end{aligned} \quad (44)$$

409 The data correction term $G(\bar{m}^{\perp})$ subtracts from the original data the component corresponding to
 410 the part of the true model that is not within the span of the basis functions. In real applications, this

411 term can never be computed since we do not know the true model \bar{m} , nor how much of it is outside
 412 the span of $\{B_l\}$. This term is therefore typically omitted and the equation solved in practice is
 413 just given by:

$$G \left(\sum_l p_l B_l \right) = d_i \quad (45)$$

414 which, combined with Equation 39, leads to the discretised inverse problem:

$$d_i = \sum_l \langle K_i, B_l \rangle p_l \quad (46)$$

415 In the seismic tomography literature, the matrix $\langle K_i, B_l \rangle$ is often denoted by G . However, we will
 416 not use that notation here since we already have a distinct (but related) use of the letter G .

417 When the number of coefficients p_l is chosen to be smaller than the number of data, such that
 418 Equation 46 is overdetermined, it is often solved in a least square (or regularised least square)
 419 manner to produce the coefficients $\{\hat{p}_l\}$. These are systematically different from the true coeffi-
 420 cients $\{\bar{p}_l\}$, because the correction term $G(\bar{m}^\perp)$ is ignored. Including more data while keeping the
 421 same basis functions $\{B_l\}$ will not eliminate the systematic error caused by omitting the correc-
 422 tion term. In order to converge to the true solution $\{\bar{p}_l\}$, one has to increase both the number of
 423 data and the number of basis functions in the expansion. Increasing the number of basis functions
 424 shrinks the space in which \bar{m}^\perp resides and thus decreases the size of the correction term $G(\bar{m}^\perp)$.
 425 Some methods exist to mitigate or eliminate the systematic error introduced by ignoring the data
 426 correction. Trampert & Snieder (1996), for example, refer to the effect of the uncorrected data as
 427 leakage, and offer a method of suppressing it based on soft priors. A different method of overcom-
 428 ing this issue is using quadratic bounds on the model space (Backus 1988a), which we will discuss
 429 in the SOLA-DLI framework.

430 The inverse problem discussed above (Equation 46) can be turned into an inference problem
 431 by defining the property mapping as:

$$[\mathcal{T}(m)]_l = \langle B_l, m \rangle_{\mathcal{M}} = p_l. \quad (47)$$

432 By also providing a model norm bound, the basis coefficients can be solved for using Equation 5.

433 As the number of data increases, the bounds on the coefficients decrease (assuming error-free
 434 data), and the mid value of these bounds approaches the true property. This contrasts with the

435 behavior of a simple least-norm solution that – without the addition of more basis functions –
436 will converge towards a systematically incorrect answer. Therefore, framing the problem as an
437 inference problem, and using norm bounds, we can avoid the “leakage problem”. This is basically
438 the same idea as that of Backus (1988a) since a norm bound is just a specific case of a quadratic
439 prior.

440 This approach and other similar ones have previously been explored by several authors (e.g.
441 Al-Attar 2021; Parker 1977), especially in the context of geomagnetic modelling problems (e.g.
442 Backus 1988a, 1989). However, these studies used mostly spherical harmonics expansions of the
443 model. In the spirit of Section 2.2, we note that the choice of target kernels (implicitly the basis
444 function expansion in this case) has an impact on the size of the property bounds (here the expan-
445 sion coefficients), which mirrors the idea that not all basis function expansions are created equal,
446 some of them being naturally better constrained by the data geometry than others.

447 Once the property bounds have been found, they can be sampled and mapped back to the
448 model space using the adjoint of the property mapping, thereby producing actual models. Since
449 this method generates a family of models rather than a single model, it is unclear which particular
450 model should be selected if one intends to run an iterative inversion based on this method.

451 **3 APPLICATIONS**

452 We use three case studies to showcase the advantages and capabilities of the SOLA-DLI method
453 introduced in the previous Section. In Case 1 (Subsection 3.1), we show the effect of the prior
454 model norm bound and choice of target kernels on the solution, illustrating how different types of
455 properties can be constrained. In Case 2 (Subsection 3.2), we illustrate SOLA-DLI can be utilised
456 to perform a simple resolution and trade-off analysis, even without data errors. Finally, in Case 3
457 (Subsection 3.3), we demonstrate how discretised model solutions can be obtained using SOLA-
458 DLI, comparing the results with a least-squares inversion solution.

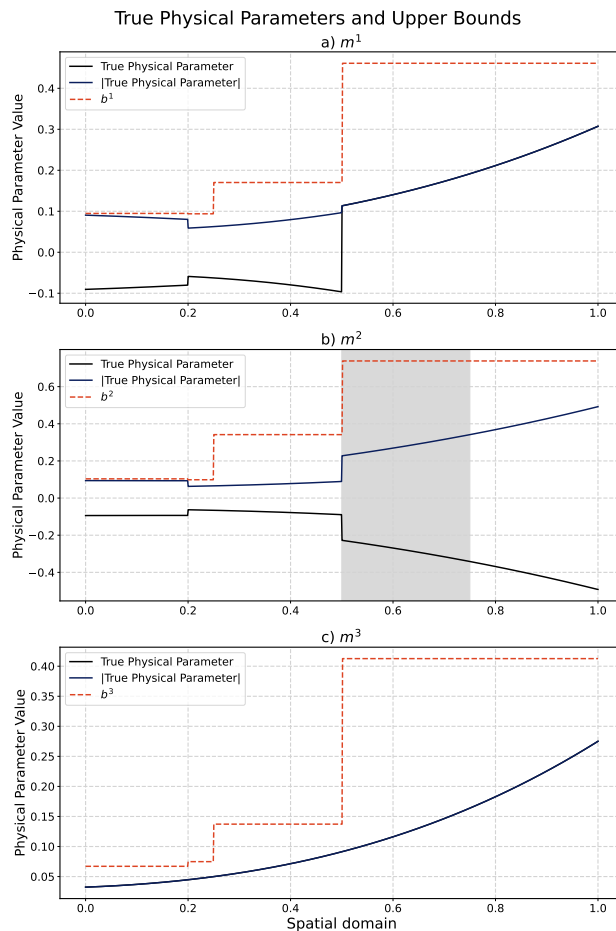


Figure 4. Case 1: True model and model norm bounds. Panels a–c show the synthetic quasi-randomly generated true model (comprised of three physical parameters) and some arbitrary piece-wise upper bound functions (b_i) used for computing the norm bound. In each panel, we present both the physical parameter (black), and the absolute value of the physical parameter (blue).

459 3.1 Case 1: Effect of Different Target Kernels

460 In this completely synthetic case study, we show how the choice of target kernels influences the
 461 inference results. We also illustrate how the prior information and the desired resolution change
 462 the local property estimates.

463 3.1.1 Setup

464 We consider a 1D model space containing three physical parameters m^1, m^2, m^3 , all of which are
 465 piece-wise continuous functions defined on the interval $[0, 1]$. The synthetic true model (Fig. 4) is
 466 generated quasi-randomly and has no physical meaning.

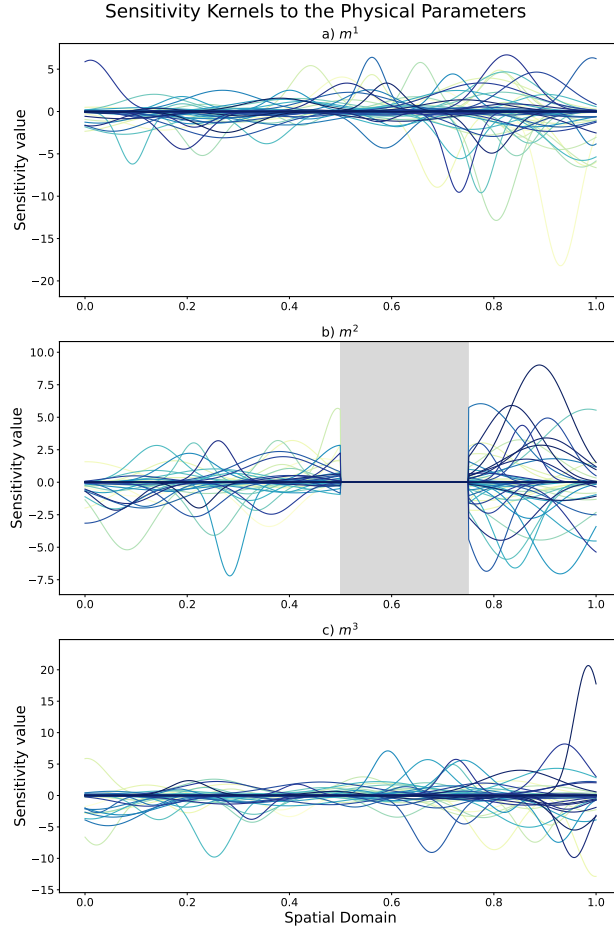


Figure 5. Case 1: Sensitivity kernels. Panels a–c show the synthetic quasi-randomly generated sensitivity kernels for physical parameters m^1, m^2, m^3 . The region with no sensitivity to m^2 is shaded in gray.

467 The model-data relationship for d_i with $i \in \{1, 2, \dots, N\}$ is given by:

$$d_i = [G(m^1, m^2, m^3)]_i = \int_0^1 K_i^1(r) m^1(r) dr + \int_0^1 K_i^2(r) m^2(r) dr + \int_0^1 K_i^3(r) m^3(r) dr \quad (48)$$

468 For each physical parameter, the sensitivity kernels are produced quasi-randomly using the equa-
469 tion:

$$K_i^j(r) = \frac{1}{\sigma\sqrt{2\pi}} \exp\left(-\frac{(r - \mu_{i,j})^2}{2\sigma^2}\right) \sin(\omega r) \sum_q c_q (r - r_q)^2 \quad (49)$$

470 where $\mu_{i,j}, c_q, r_q, \omega$ are randomly generated (see Fig. 5). We choose to use $N = 150$ (e.g. 150
471 observations) with the sensitivity kernels computed for each physical parameter. To simulate the
472 lack of data sensitivity to a particular region (e.g. no S-wave sensitivity in the Earth's outer core),
473 we manually set the sensitivity kernels for m^2 to zero in the interval $[0.5, 0.75]$. The synthetic

474 (error-free) data are then produced using Equation 48 combined with the synthetic sensitivity
 475 kernels and the synthetic true model. As target kernels we use those defined in Equations 26, 27
 476 and 28 choosing a width of 0.2.

477 The least norm solution to this problem (Equation 48) is given by the Moore-Penrose right-
 478 inverse:

$$\tilde{m} = G^*(GG^*)^{-1}d \quad (50)$$

479 and shown in Fig. 6. This is a regularised inverse solution obtained by selecting the solution with
 480 the least norm from the set of all possible solutions. We note that in this case the least norm solution
 481 approximates the true model reasonably well, except in the regions with no sensitivity (where the
 482 solution is set equal to zero), indicating that the true model norm is very close to the least norm.

483 To solve the SOLA-DLI inference problem, upper bound functions b^i are chosen arbitrarily
 484 (Fig. 4) such that:

$$|m^j(r)| \leq b^j(r) \quad \forall r \in [0, 1], \quad (51)$$

485 which leads to the following upper bound on the model norm:

$$\|m^j\|_{\mathcal{M}^j} = \sqrt{\int_0^1 (m^j)^2 dr} \leq \sqrt{\int_0^1 (b^j)^2 dr} = M^j \quad (52)$$

$$\|m\|_{\mathcal{M}} \leq M = M^1 + M^2 + M^3 \quad (53)$$

486 In real applications, the upper bound functions b^j should be chosen carefully based on physi-
 487 cal arguments, for example using constraints from mineral physics, as discussed already in Sec-
 488 tion 2.1.2.

489 3.1.2 *Local Averages and Gradients*

490 As introduced in Section 2.2, we consider three types of local averages (uniform local averages,
 491 Gaussian averages, and bump averages) and three types of locally averaged gradients (triangular
 492 averaged gradients, bump averaged gradients, and Gaussian averaged gradients). In this case study,
 493 we are specifically interested in obtaining these properties for parameter m^2 given its region of no

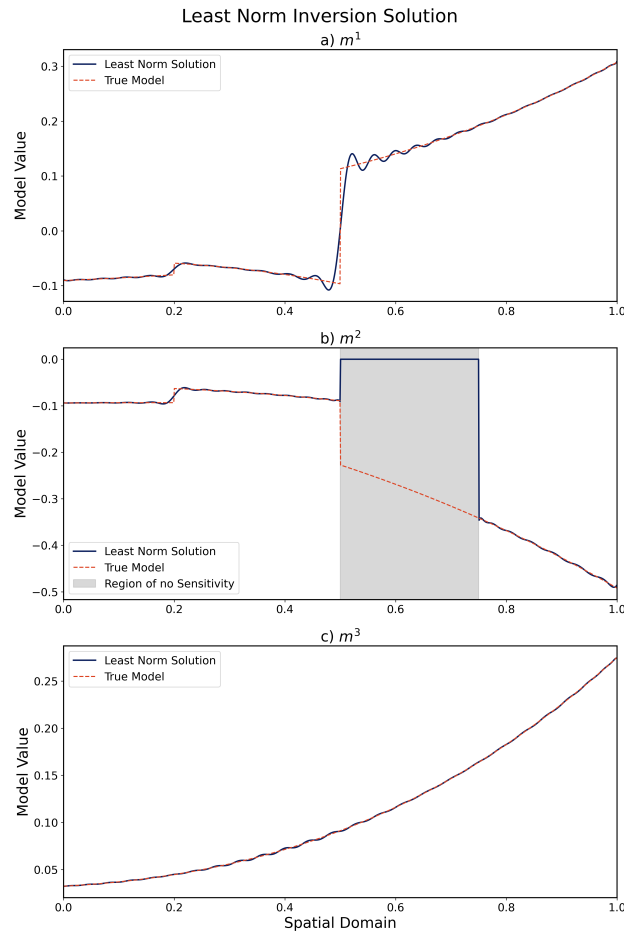


Figure 6. Case 1: Least norm solution for (m^1, m^2, m^3) obtained using Equation 48.

494 sensitivity. We evaluate the properties at 100 equally spaced inquiry points in the spatial domain,
 495 with the results plotted in Fig. 7 and Fig. 8.

496 For each type of property, at each of the 100 enquiry points, the solution (Equation 23) pro-
 497 vides both an upper and a lower bound. Figure 7 shows that the uniform local average is the least
 498 constrained property, while the Gaussian average is the best constrained. This result is not sur-
 499 prising, given that the sensitivity kernels are Gaussians modulated by polynomial and sinusoidal
 500 functions. If the sensitivity kernels were more similar to boxcar functions, we should expect the
 501 uniform local averages to be better constrained.

502 Regions with no sensitivity are poorly constrained, as here the only constraint comes from
 503 the model norm bound. While it is unsurprising that some properties are better constrained than
 504 others, it is particularly notable that the property bounds for the local averages are so large that
 505 they provide little information about the true property values, even in regions with data sensitivity.

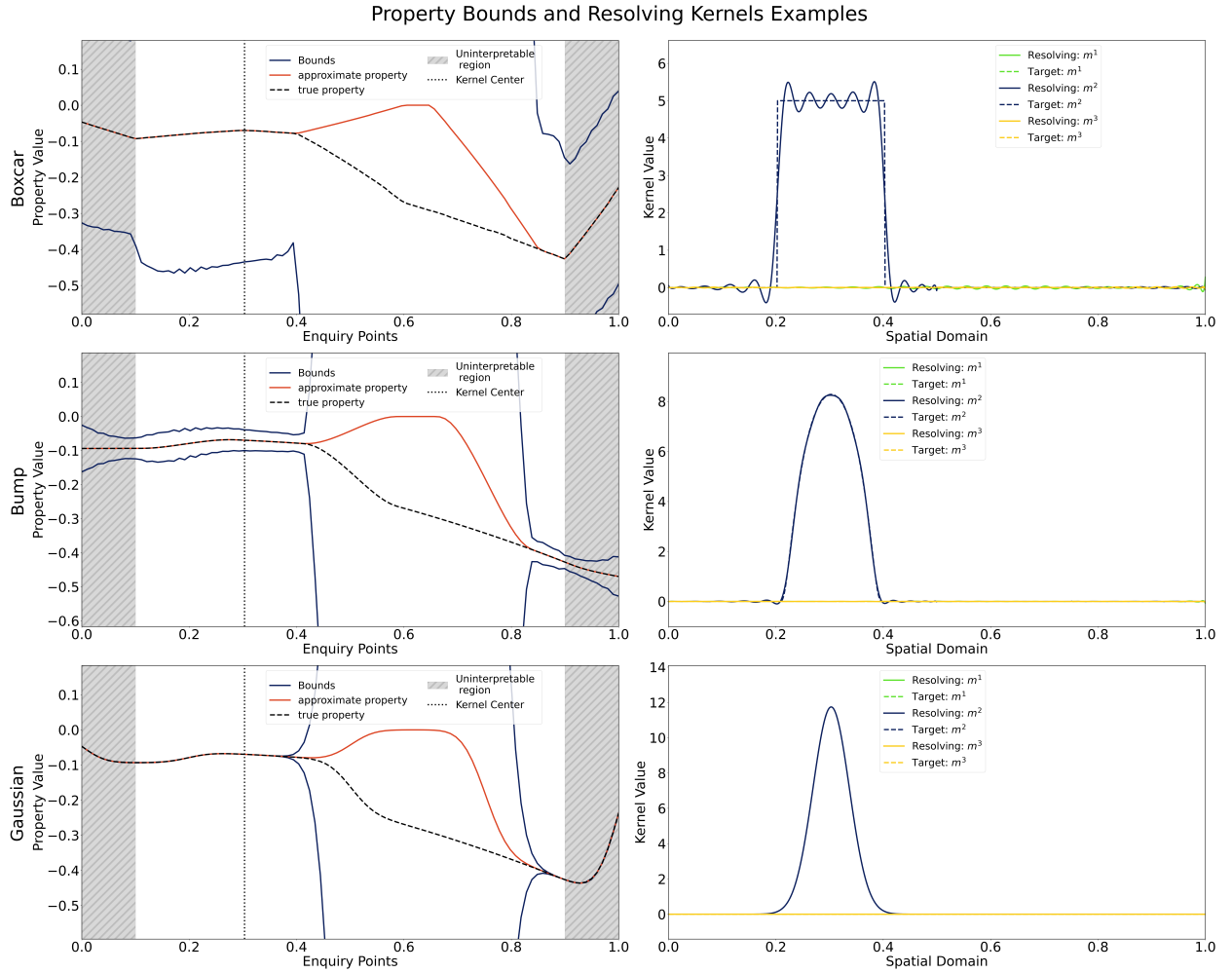


Figure 7. Case 1: SOLA-DLI solutions for three different types of local average properties. First column: solution bounds for three types of local averages of physical parameter m^2 evaluated at 100 evenly spaced enquiry points. Second column: target and resolving kernels for each type of property at the enquiry point located at $r^k = 0.3$ with width 0.2. The approximate property represents the SOLA solution in the absence of the unimodularity condition, which is mathematically just the true model mapped through the approximate mapping \mathcal{R} .

506 Conversely, the Gaussian averages yield such tight bounds that we can be highly confident in the
 507 actual property values, assuming that the prior information is correct. These distinct differences
 508 in the ability to constrain the property are significant, as we are often interested in extracting
 509 meaningful information about the true model, rather than obtaining a specific type of average.
 510 Thus, it is important to recognize that the choice of averaging type can significantly impact how
 511 much information is obtained.

512 When we aim to obtain locally averaged gradients as properties, smoother target kernels again

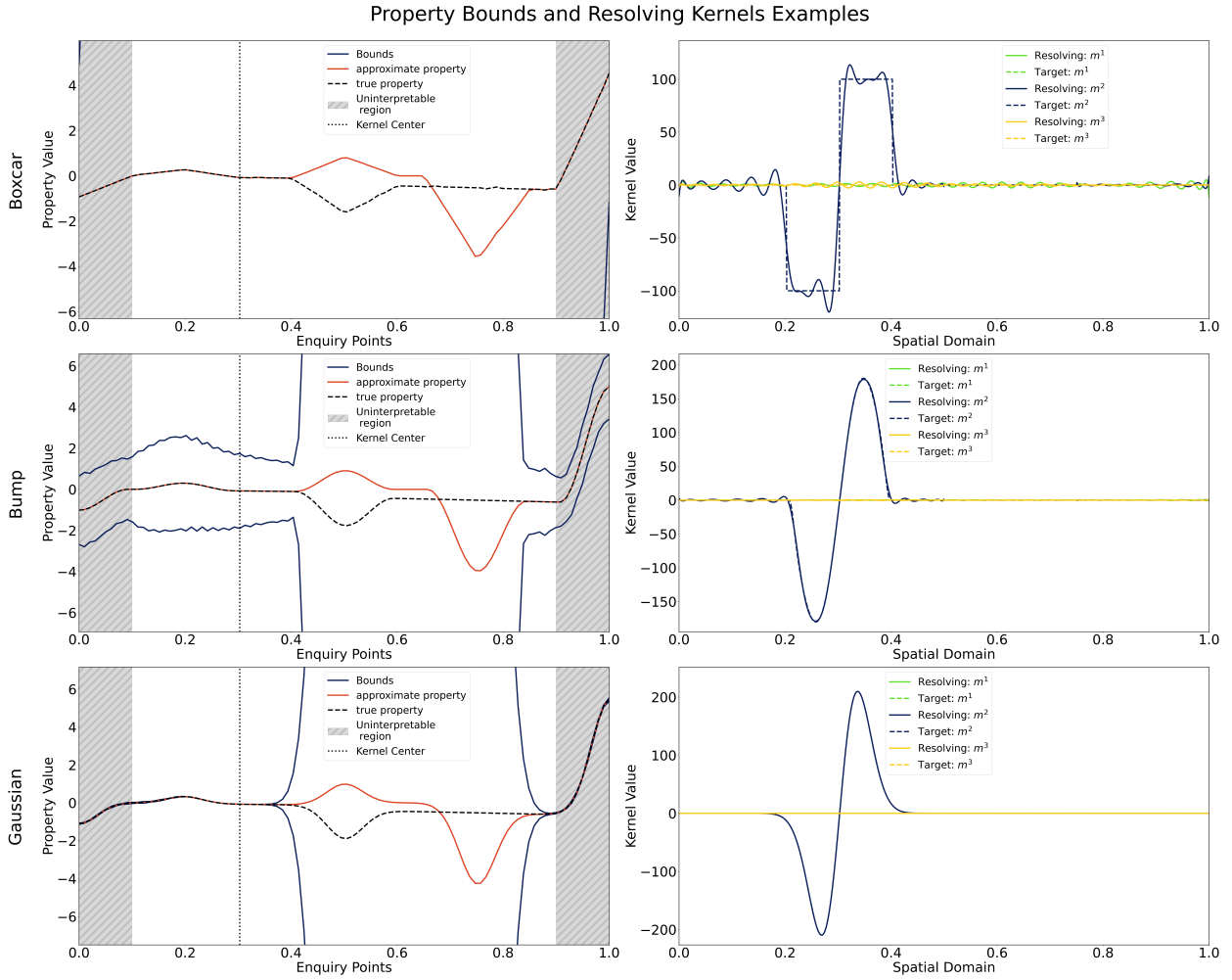


Figure 8. Case 1: SOLA-DLI solutions for three different types of local averaged gradient properties, similar to Fig. 7.

513 lead to significantly better property bounds (Fig. 8), similar as noted for local averages. Notice
 514 however, that while the resolving kernels look similar, the property bounds of the gradients are
 515 typically larger than for the averages (compare Fig. 7 and Fig. 8).

516 In the absence of unimodularity conditions, the SOLA solution (“approximate property”) is
 517 obtained by mapping the true model through the approximate mapping \mathcal{R} . Because the true model
 518 is close to the least norm model, a comparison between the true and approximate property values
 519 will give the false impression that it outperforms the DLI method. However, we must remember
 520 that approximate property values do not provide us the desired information about the true property
 521 values. In addition, the approximate property values must be interpreted through the resolving
 522 kernels, which can be rather different from the target kernels, and also vary in shape from one

523 enquiry point to another. Furthermore, we believe that the SOLA method also benefits from better
 524 designed target kernels, as they can lead to better resolving kernels and an easier interpretation of
 525 the results.

526 *3.1.3 Effect of the prior model norm bound*

527 When we change the norm bound prior information, only the property error bounds are affected
 528 (see Equation 24). This is illustrated in Fig. 9, where we show results for three different upper
 529 bounds on the true model. Bound 3 is the most conservative, assuming a constant function three
 530 times larger than the maximum of the true physical parameter. Bounds 1 and 2 are tighter and
 531 therefore assume more prior knowledge. The bottom panel of the same figure illustrates that,
 532 as expected, tighter norm bounds lead to tighter property bounds. In all cases, the range remains
 533 centered on the approximate property. It is interesting to note that restricting the bounding function
 534 b^j in some local region does not lead to a tighter property bounds at an enquiry point in the same
 535 region, but rather it will lead to a uniform decrease of the property bounds at all enquiry points.

536 *3.1.4 Effect of target kernel width*

537 Changing the width of the target kernels can be interpreted as changing the resolution of the
 538 property evaluated at a given enquiry point. To investigate this, we have varied the target width
 539 between 1% and 100% of the domain width and computed the relative error bounds for all the
 540 enquiry points and widths. The results are plotted in Fig. 10. The relative error bound shown in the
 541 first column is defined as:

$$e^{(k)} = \frac{\epsilon^{(k)}}{\max(\tilde{p}) - \min(\tilde{p})} \quad (54)$$

542 where \tilde{p} is the property of the least norm model solution \tilde{m} . This metric has been chosen as the
 543 absolute error ϵ is not a good metric for determining whether a property is well constrained, while
 544 the classic relative error defined as ϵ/\bar{p} cannot be computed without knowing the true property \bar{p} .
 545 While there is no quantitative rule for what constitutes an unacceptable high relative property error
 546 bound, we believe any relative error higher than 100% is “certainly too high”, and relative errors
 547 less than 10% are “generally good”.

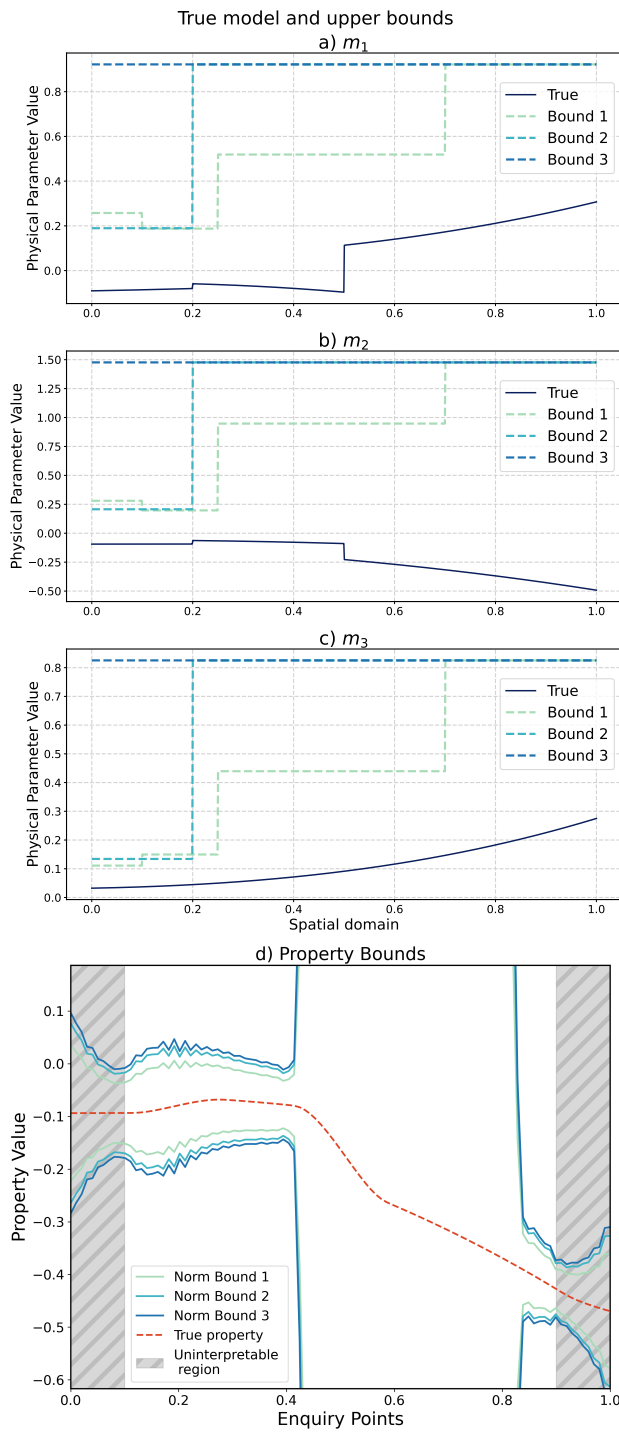


Figure 9. Case 1: Effect of prior norm bound on the property bounds. a–c) indicate the levels of three different upper bounds on all three model parameters of the true model. Our choice of norm bound functions results in the following prior norm bounds (M^i): 2.44 (Bound 1), 3.89 (Bound 2) and 4.34 (Bound 3), which are all larger than the true model norm of 0.32. d) Solutions corresponding to the three different model upper bounds, using a bump average for m^2 as example. Tighter norm bounds lead to tighter constraints on the desired properties.

548 In general, we find that for all target kernel types the relative error bounds increase when
 549 we decrease the width of the target kernel (i.e. increase resolution). In addition, regions with no
 550 sensitivity always lead to large relative errors. As expected, the width of the uninterpretable regions
 551 at the edge of the domain increases with larger target kernel width (decreasing resolution) as the
 552 half-width of the kernel increases. Finally, in this setup, we find that particular properties, e.g.
 553 Gaussian averages, are constrained better (i.e. lower relative error bounds) than uniform or bump
 554 local averages, for all enquiry points and for target kernel widths (i.e. all resolutions), likely due
 555 to the fact that Gaussian-like sensitivity kernels were used.

556 This case study illustrates the general notion that we typically use inference methods to answer
 557 specific questions about a true model rather than finding the entire model itself. In SOLA-DLI,
 558 these questions are encoded in our chosen target kernels, which should be carefully designed to
 559 improve the property bounds and facilitate straightforward interpretations. The differing extent to
 560 which we are able to retrieve different target kernels effectively shows that our data can answer
 561 some questions better than others.

562 **3.2 Case 2: Quasi Synthetic Normal Mode Application**

563 In this quasi-synthetic case study, we illustrate how to use SOLA-DLI to conduct a simple reso-
 564 lution analysis without real data or model values nor any prior information, based solely on the
 565 sensitivity kernels of the data set. We also illustrate how the results of such a resolution analysis
 566 can be linked to trade-offs between physical parameters.

567 *3.2.1 Setup*

568 We consider a model formed by the triplet $m = (\delta \ln(v_s), \delta \ln(v_p), \delta \ln(\rho))$, where v_s is shear-
 569 wave speed, v_p is compressional-wave speed, and ρ is density (Fig. 11). Each physical parameter
 570 is assumed to be a piece-wise continuous function defined over the interval $[0, R_E]$ where R_E is
 571 Earth's radius (approximately 6371 km). We aim to constrain Gaussian averages and gradients of
 572 this synthetic true model using realistic normal mode sensitivity kernels (Woodhouse & Dahlen
 573 1978). Specifically, we select the same modes as in the SP12RTS dataset (Koelemeijer et al. 2016;

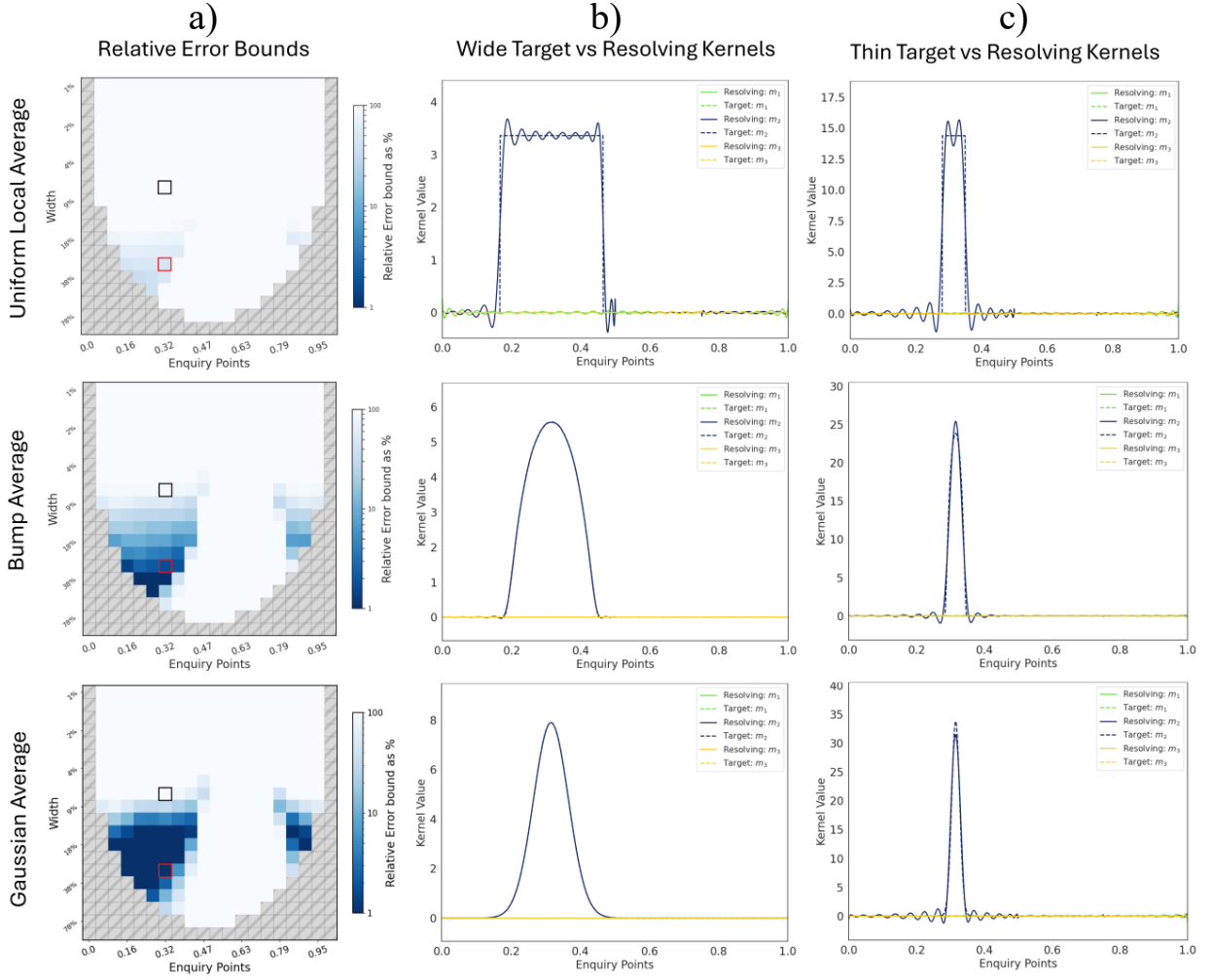


Figure 10. Case 1: Relative error bounds with examples of resolving kernels compared to their target kernels. The different rows correspond to different types of target kernels, e.g. uniform local average (top), bump average (middle) and Gaussian average (bottom). In the three columns, we show (a) the relative error bounds e ; (b) examples for wide target and resolving kernels, corresponding to the red squares in (a) and (c) examples for narrow target and resolving kernels, corresponding to the black squares in (a).

574 Restelli et al. 2024), i.e. 143 modes with their sensitivity to $\delta \ln(v_s)$, $\delta \ln(v_p)$ and $\delta \ln(\rho)$ concen-
 575 trated mostly in the mantle (see Fig. 12).

576 3.2.2 Resolution Analysis

577 Before introducing any data or model values, we are able to perform a simple resolution analysis to
 578 investigate where and on what spatial scale our data contain information regarding the Earth model.
 579 While the SOLA-DLI solution itself depends on the model norm bound via M (see Equation 24),
 580 indirectly on the data via $\|\tilde{m}\|_{\mathcal{M}}$ (see Equation (25)), and on the relationships between the target

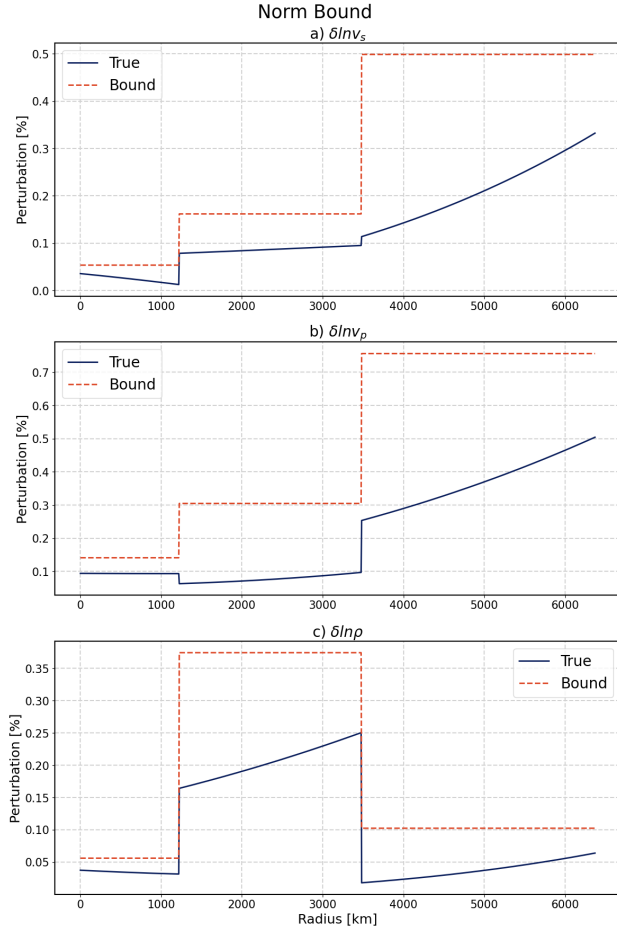


Figure 11. Case 2: Arbitrary quasi-random synthetic true model and the upper bound functions used to compute the prior upper bound norm.

581 kernels and sensitivity kernels via \mathcal{H} (see Equations D.14–D.23), the resolving kernels only depend
 582 on the data geometry, i.e. the data sensitivity kernels.

583 The diagonal elements of the matrix \mathcal{H} can be shown to equal:

$$\mathcal{H}_{kk} = \sum_j^{N_m} \|T^{j,(k)} - A^{j,(k)}\|_{\mathcal{M}_j}^2 \quad (55)$$

584 which essentially quantifies the cumulative difference between our target and resolving kernels.

585 Using \mathcal{H} we can also define the resolving misfit as a more useful metric:

$$R_k = \frac{\sqrt{\mathcal{H}_{kk}}}{\sum_j^{N_m} \|T^{j,(k)}\|_{\mathcal{M}_j}} = \frac{\sqrt{\sum_j^{N_m} \|T^{j,(k)} - A^{j,(k)}\|_{\mathcal{M}_j}^2}}{\sum_j^{N_m} \|T^{j,(k)}\|_{\mathcal{M}_j}} \quad (56)$$

586 which is a generalisation of the “resolution misfit” defined in Restelli et al. (2024). The resolving
 587 misfit is 0 when all the resolving kernels associated with some property evaluated at $r^{(k)}$ are equal
 588 to the corresponding target kernels. This would mean that our data contain exact information about

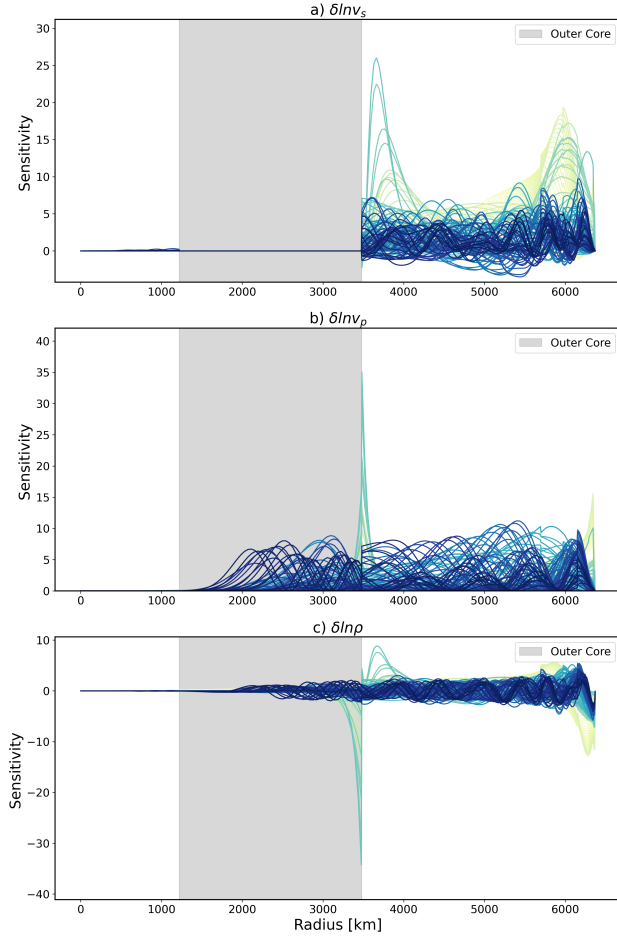


Figure 12. Case 2: Normal mode sensitivity kernels for a) $\delta \ln(v_s)$, b) $\delta \ln(v_p)$ and c) $\delta \ln(\rho)$, obtained using a modified version of OBANI based on the work of Woodhouse & Dahlen (1978). The shaded region indicates the depth range of the outer core, where the sensitivity to v_s is zero.

589 the desired property and the property error bounds are 0. On the other hand, the resolving misfit
 590 is equal to 1 when our resolving kernels are zero, which would correspond to a complete lack
 591 of sensitivity of our data to the desired property. It is important to note that the computation of
 592 the resolving misfit does not use the data vector d nor any prior model information, it only uses
 593 the “geometry of the data set” (Latallerie et al. 2024). Fig. 13 illustrates the information that is
 594 provided by the resolving misfit (left column). As indicated by a low resolving misfit (darker
 595 shades of blue), our data mostly contain information in the mantle, as expected from this selection
 596 of sensitivity kernels. The resolving misfit is also typically low for wide target kernels ($>18\%$
 597 domain width, or more than 1000 km). Wide gradient kernels can be better recovered in the mantle,

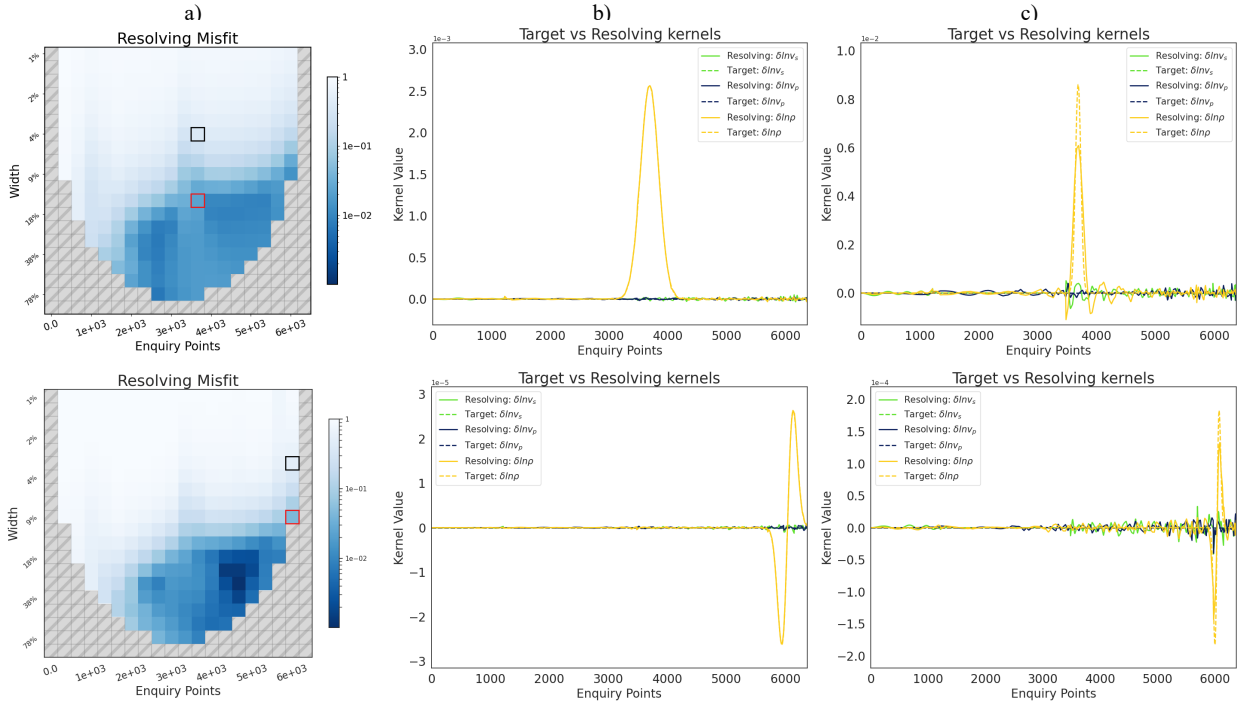


Figure 13. Case 2: Resolution analysis for a Gaussian average (top) and gradient (bottom) target for $\delta \ln(\rho)$ using realistic mode sensitivity kernels. The resolving misfit (left) and kernels (middle and right) can be computed without the need for data or any prior norm bound information. The middle and right panels illustrate the target and resolving kernels for a wide and thin target, including the contaminant kernels that indicate trade-offs between physical parameters.

598 while wide averaging kernels can be better recovered in the lower outer core, again indicating that
 599 our choice of target (i.e. property) is important.

600 3.2.3 Trade-offs between physical parameters

601 When our data are sensitive to two or more physical parameters, it may become difficult or im-
 602 possible to obtain properties of a single parameter in isolation from the others. These trade-offs
 603 between physical parameters pose problems for interpretations, particularly in regions such as the
 604 lower mantle where the sensitivity of normal modes to seismic velocities and density is similar.

605 Our setup with SOLA-DLI, where we explicitly set the target kernels for parameters not of
 606 interest to zero, enables us to easily visualise and consider model parameter trade-offs. Suppose
 607 we are interested in some local property of $\delta \ln(\rho)$, for example the Gaussian local average density
 608 in the deep mantle or the density jump across the 660 discontinuity as characterised by a Gaussian

609 gradient (Lau & Romanowicz 2021). If we choose low resolution (wide) target kernels (middle
 610 column), we find that the resolving kernels for $\delta \ln(\rho)$ match the target kernels well (Fig. 13). Fur-
 611 thermore, the resolving kernels for $\delta \ln(v_s)$ and $\delta \ln(v_p)$ also match their respective target kernels,
 612 which are just zero. Such zero or near zero resolving kernels indicate that the trade-off between the
 613 physical parameter of interest and the other physical parameters is small. However, if we choose
 614 higher resolution (thin) target kernels (right column), we notice that the resolving kernels are strug-
 615 gling to match their respective target kernels. The resolving kernels for $\delta \ln(v_p)$ and particularly
 616 $\delta \ln(v_s)$ are far from zero, indicating significant trade-offs with the desired property of density,
 617 which are regarded as *contaminants*. Such trade-offs between physical parameters are naturally
 618 taken into account by SOLA-DLI and typically result in higher error bounds on the property. If
 619 instead we would account for the sensitivity to $\delta \ln(v_p)$ and $\delta \ln(v_s)$ by scaling the sensitivity ker-
 620 nels, we would obtain tighter bounds, at the expense of assuming more prior information, similar
 621 to the results of Restelli et al. (2024) using the “3D noise” approach in their SOLA inversions.

622 3.3 Case 3: Discretised inversions using continuous SOLA-DLI

623 This final case study serves to illustrate how we can obtain a family of discretised model solutions
 624 using SOLA-DLI, and how this approach compares to a typical least-squares inversion model
 625 solution.

626 3.3.1 Setup

627 Here, we consider a model m with only one physical parameter, denoted also m (see the true
 628 model in Fig. 14 a)). Our model space \mathcal{M} is $PCb[0, 1]$ and the data are given by:

$$d_i = \langle K_i, m \rangle_{\mathcal{M}} \quad (57)$$

629 where K_i are some quasi-randomly functions, generated again using Equation 49 (see Fig. 14 b)).

630 In this setup, we choose to discretise the model using a Fourier expansion. The resulting basis

631 functions are (see Fig. 14 c)):

$$B_l(r) = \begin{cases} 1, & l = 0 \\ \sqrt{2} \sin(2\pi \frac{l+1}{2} r), & l \text{ odd} \\ \sqrt{2} \cos(2\pi \frac{l}{2} r), & l \text{ even} \end{cases} \quad (58)$$

632 and a possible model expansion with Fourier coefficients p_l is given by:

$$m(r) \approx \sum_l p_l B_l(r). \quad (59)$$

633 The discretised model–data relation used for the least-squares inversion is:

$$d_i = \sum_l \langle K_i, B_l \rangle_{\mathcal{M}} p_l = \sum_l \Gamma_{il}^* p_l, \quad (60)$$

634 where (see also Appendix D2):

$$\Gamma_{ij}^* = \langle K_i, B_j \rangle_{\mathcal{M}}. \quad (61)$$

635 This leads to the following least-squares solution for p_l :

$$\hat{p} = (\Gamma \Gamma^*)^{-1} \Gamma d \quad (62)$$

636 Using the least-squares solution $\{\hat{p}_l\}$, we can thus find the corresponding model solution by using

637 the Fourier expansion:

$$\hat{m} = \sum_l \hat{p}_l B_l. \quad (63)$$

638 To obtain the SOLA-DLI solution, we consider the Fourier coefficients p_l to be elements of a

639 property vector obtained from the property mapping:

$$p_l = [\mathcal{T}(m)]_l = \langle B_l, m \rangle_{\mathcal{M}}. \quad (64)$$

640 We also introduce a prior model norm bound (see Fig. 14 a)). This leads to the following SOLA-

641 DLI problem:

Given

$$d_i = \langle K_i, m \rangle_{\mathcal{M}} \quad (65)$$

Find

$$p_l = \langle B_l, m \rangle_{\mathcal{M}}. \quad (66)$$

642 This problem is readily solved using Equation 23 to obtain upper and lower bounds for the possible
643 values of the Fourier coefficients:

$$\bar{p}_l \in [\tilde{p}_l - \epsilon_l, \tilde{p}_l + \epsilon_l]. \quad (67)$$

644 In this case \tilde{p}_l are the Fourier coefficients of the least norm solution to Equation 57, which are not
645 to be confused with the single least-squares solution \hat{p}_l . In contrast, the property bounds obtained
646 from SOLA-DLI (Equation 67) offer a family of solutions that can be sampled.

647 3.3.2 Discretised least-squares vs. SOLA-DLI solution

648 We compute both the least-squares and discretised SOLA-DLI solution using different number
649 of data points (50, 70 or 100), solving for 29 Fourier coefficients. SOLA-DLI initially provides
650 property bounds on the Fourier coefficients, and we therefore have to draw samples from these
651 distribution for each Fourier coefficient distribution to obtain a possible model solution, illustrated
652 in Fig. 15.

653 When using few data (Fig. 15, the least-squares inversion generally struggles to retrieve Fourier
654 coefficients close to the true ones, while the bounds of the SOLA-DLI solution always encompass
655 the true coefficients (true properties). That said, for certain Fourier coefficients and in certain
656 parts of the model, the least-squares solution does appear to approach the true property (Fourier
657 coefficients) and the true model better than the SOLA-DLI solution. Increasing the number of data
658 to 70 leads to a better least-squares solution, especially for the first 10 Fourier coefficients, and
659 tighter bounds of the SOLA-DLI solution. However, it now becomes clear that the SOLA-DLI
660 bounds offer more accurate information, always encompassing the true Fourier coefficients and
661 better resembling the true model compared to the least-squares solution. When we further increase

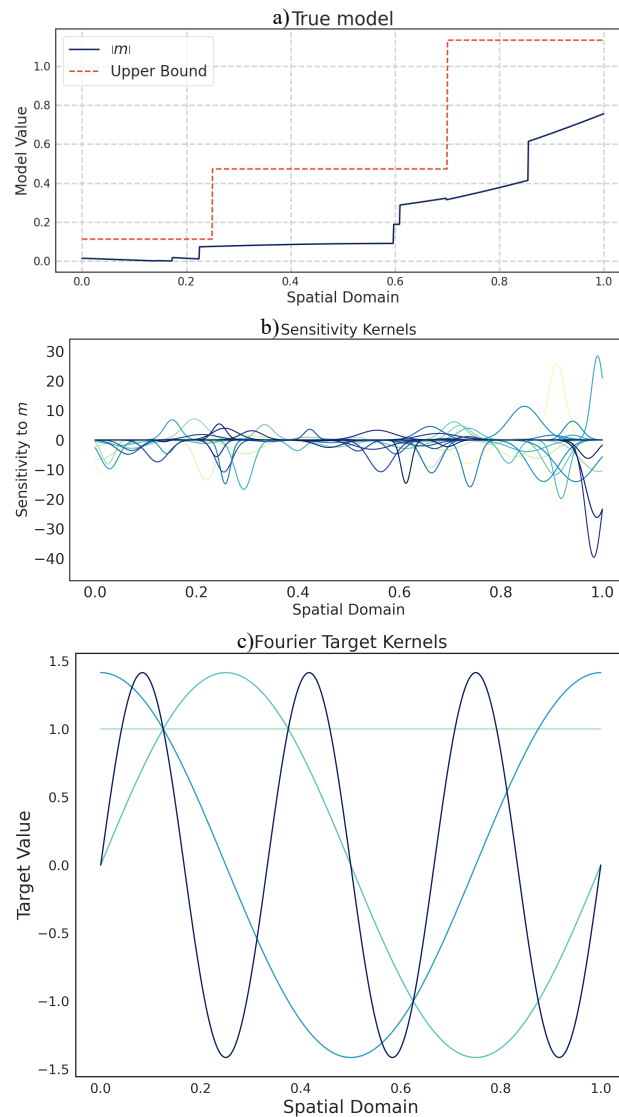


Figure 14. Case 3: Model setup and kernels. (a) True model m with the upper bound function used to compute the prior model norm bound. (b) Synthetic quasi-random sensitivity kernels. (c) Examples of four Fourier basis functions.

662 the number of data points to 100 (see Figs. 15 c) and f)), we note that the SOLA-DLI solution
 663 converges closely to the true Fourier coefficients and model, while the least-squares inversion
 664 systematically deviates.

665 In our synthetic setup, it is possible to explicitly compute the data correction term, which
 666 captures the components of the true model that are not within the span of the basis functions (see
 667 Section 2.4, Equation 2.4). When we correct the data, using our knowledge of the true model, we
 668 find that the least-squares inversion solution converges to the true Fourier coefficients, even for

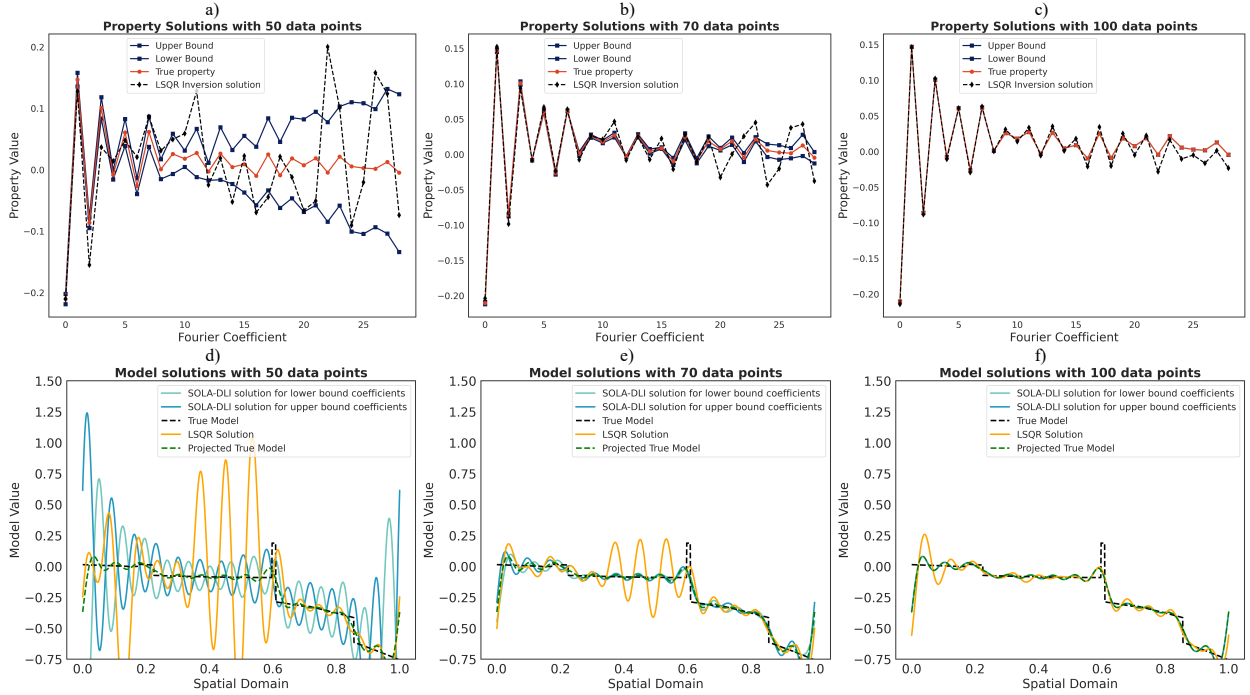


Figure 15. Case 3: Comparison between least-squares and SOLA-DLI solution for a model discretised using Fourier basis functions. a–c) Fourier coefficients from discretised least-squares inversion and bounds of the SOLA-DLI solution using a) 50 data points, b) 70 data points and c) 100 data points. d–f) Discretised model solution from discretised least-squares and two samples from the SOLA-DLI property bounds using d) 50 data points, e) 70 data points and f) 100 data points.

669 few data (Fig. 16). This demonstrates the equivalence of the discretised least-squares and SOLA-
 670 DLI solutions. However, in real world applications, when the true model is unknown, this data
 671 correction term cannot be computed. Consequently, the SOLA-DLI solution should be preferred
 672 over the discretised least-squares inversion method. As mentioned before, there are other methods
 673 (e.g. Trampert & Snieder 1996) for bypassing or approximating the effect of the data correction
 674 term, which should also be preferred over a simple least norm inversion.

675 4 DISCUSSION

676 In this contribution, we have introduced the SOLA-DLI framework, which combines the advan-
 677 tages of both DLI and SOLA branches of inferences. At present, we have focused on error-free
 678 data, as the fundamental distinction between the two branches lies in their treatment of uncer-
 679 tainties arising from incomplete data, not from how data noise is incorporated. However, for any

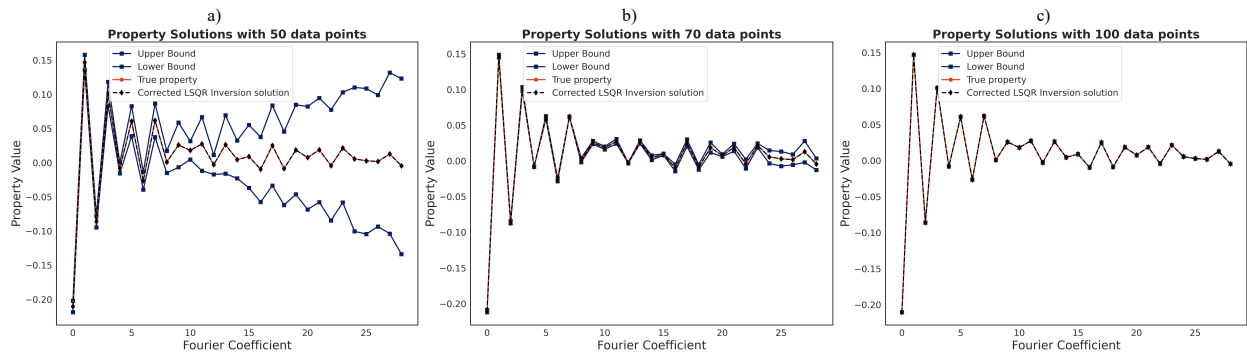


Figure 16. Case 3: Comparison between Fourier coefficients obtained using SOLA-DLI and the discretised least-squares method with an additional data correction term, using a) 50 data points, b) 70 data points and c) 100 data points. A comparison with the least-squares solutions in Fig. 15 indicates that the data correction leads to the systematic error in the Fourier coefficients.

680 real-world application, it is essential to address data noise. Al-Attar (2021), Parker (1977), and
 681 Backus (1970a) have each proposed methods for incorporating noise into DLI-based approaches.
 682 Since the SOLA-DLI framework integrates both methodologies, we can draw upon these exist-
 683 ing approaches and adapt them as necessary to introduce data noise into the framework. There
 684 are numerous ways to achieve this, but it is not yet clear which approach would best balance
 685 computational efficiency with the need to produce property bounds that are not excessively large.
 686 Depending on the chosen approach, the matrix X may be affected by noise, which would alter the
 687 final form of the resolving kernels. However, this does not render them unusable or uncomputable,
 688 and crucially, it does not alter their interpretation. We believe that the selection of target kernels
 689 also remains important, but in the presence of data noise, a particular set of target kernels A may
 690 perform better than another set B , whereas in the absence of noise, set B might outperform set A .
 691 This variability does not undermine the points that we make in the present contribution, which is
 692 that some target kernels are more effective than others. A potential direction for future research
 693 could be target optimisation, where, given a set of data, the goal is to identify those target ker-
 694 nels that produce the most effective constraints from a family of, for example, averaging weight
 695 functions. We anticipate that the methods behind such an optimisation algorithm would need to
 696 account for data noise.

697 We expect that the careful treatment of target kernels will become more involved when going

698 to 2D or 3D cases (e.g. Zaroli 2016; Latallerie et al. 2022; Freissler et al. 2024). However, it
 699 also opens up more possibilities. In higher dimensions, we can design target kernels sensitive to
 700 directional gradients or local curvature using kernels that represent smoothed Laplacian operators.
 701 Such target kernels would for example amplify the presence of a gap between two peaks rather
 702 than smoothing the peaks into one, which could be useful for studying plumes (similar to the idea
 703 of point-spread functions of Fichtner & Trampert (2011)). Another possible extension of our work
 704 would be to replace the deterministic prior information with probabilistic information by placing
 705 a prior measure on the model space, which can be updated using noisy data measurements and
 706 propagated into the property space. Backus (1970a) already mentioned such a modification and
 707 Al-Attar (2021) added to this discussion. Such a modification would lead to yet another possible
 708 mechanism for dealing with data noise.

709 The introduction of prior model information via the model norm bound is of great importance
 710 in the SOLA-DLI method. The model norm bound (L_2 norm) chosen here is the most common due
 711 to its mathematical simplicity, but as pointed out by Al-Attar (2021) and discussed in Section 2.1.2,
 712 there might be better prior constraints. Other model norms may allow to place bounds on the
 713 maximum point-value of the true model, or its gradients (smoothness) (Stark & Hengartner 1993).
 714 Such modifications may necessitate the use of more general spaces than Hilbert spaces, which
 715 adds significant theoretical complications. We refer the interested reader to Al-Attar (2021) for the
 716 required theoretical modifications.

717 The computational cost of the methods presented arises from multiple sources. Computing the
 718 matrices Λ ($N_d \times N_d$) and Γ ($N_p \times N_d$) requires at most $N_m(N_d^2/2 + N_p N_d)$ integrations for N_m
 719 model parameters, with the cost depending on the sensitivity and target kernels used. Sensitivity
 720 kernels, especially in the case of finite-frequency adjoint methods, can be expensive to compute. If
 721 sensitivity kernels already exist, the integration cost for SOL-DLI depends only on the number of
 722 kernels and the integration scheme. Since Λ^{-1} is rarely computed explicitly, applying it involves
 723 solving $N_p + 1$ linear systems, similar to the cost of obtaining a SOLA or DLI solution without data
 724 noise (Al-Attar 2021), and much lower than the classic Backus-Gilbert method (Backus & Gilbert
 725 1970; Pijpers & Thompson 1992). For SOLA-DLI, these $N_p + 1$ solves yield the final solution,

while normal DLI requires additional computations involving \mathcal{H}^{-1} to assess the hyperellipsoid constraints. When accounting for data noise, the cost depends on the method used to incorporate it, which will likely be adapted from existing SOLA or DLI approaches. Thus, the total cost of SOLA-DLI is expected to be comparable to DLI or SOLA, making it computationally attractive for inference problems.

5 CONCLUSION

In this contribution, we have presented the theory and possible applications of the SOLA-DLI framework, which combines the Backus-Gilbert based SOLA method with Deterministic Linear Inferences (DLI). To derive this framework, we have first demonstrate the links between these two branches of inference methods, before showing how the combined framework is capable of providing a more comprehensive analysis. We have particularly emphasised the distinction between interpreting results through target kernels versus resolving kernels. As a result, target kernel design is significantly more important in SOLA-DLI. In addition, the framework is capable of incorporating multiple physical parameters, with trade-offs captured by contaminant kernels. Furthermore, we have demonstrated how discretised models can be obtained using these linear inference methods, highlighting the advantages and disadvantages associated with different approaches. All of these theoretical aspects are practically demonstrated through three synthetic, noise-free case studies, with software provided to enable the reader to explore these further themselves.

6 ACKNOWLEDGEMENTS

We thank the Editor (Carl Tape), Malcolm Sambridge and an anonymous reviewer for their comments, which have substantially improved the manuscript. AMM is funded by a NERC DTP studentship NE/S007474/1 and gratefully acknowledges their support. AMM also received funding from Royal Society grant RF\ERE\210182 awarded to PK. CZ acknowledges financial support from ITES (Institut Terre et Environnement de Strasbourg, UMR 7063) for a research visit to Oxford. PK acknowledges financial support from a Royal Society University Research Fellowship (URF\1\180377). Normal mode sensitivity kernels were computed using a modified version of

752 OBANI, which is based on the work of Woodhouse & Dahlen (1978). The authors thank Sam
 753 Scivier, Franck Latallerie and David Al-Attar for fruitful theoretical discussions. The following
 754 Python packages were used extensively for producing and plotting the synthetic data: Scipy (Vir-
 755 tanen et al. 2020), Numpy (Harris et al. 2020) and Matplotlib (Hunter 2007). For the purpose of
 756 Open Access, the author has applied a CC BY public copyright licence to any Author Accepted
 757 Manuscript (AAM) version arising from this submission.

758 **7 DATA AVAILABILITY**

759 The sensitivity kernels and all the codes used to produce the figures in this paper can be found at
 760 https://github.com/Adrian-Mag/SOLA_DLI (Mag et al. 2024).

761 **APPENDIX A: OVERVIEW OF INFERENCE METHODS**

762 In this appendix, we present an informal overview of inference methods in the absence of data
 763 noise. We consider the most general form of an inference problem to be (see also Fig. 1b):

Given:

$$G(\bar{m}) = d$$

Find:

$$\mathcal{T}(\bar{m}) = \bar{p}$$

where

$$G : \mathcal{M} \rightarrow \mathcal{D}$$

$$\mathcal{T} : \mathcal{M} \rightarrow \mathcal{P}$$

764 The true model \bar{m} is unknown, and we only have data constraints at our disposal to find some
 765 properties \bar{p} of that true model. In general, there are six choices we have to make before attempting
 766 to solve this problem: we must decide what $G, \mathcal{T}, \mathcal{M}, \mathcal{D}, \mathcal{P}$ are, and whether we want to introduce
 767 prior information or not, which we will discuss below.

A1 Choice of \mathcal{D} , \mathcal{P} , \mathcal{M} and \mathcal{T}

For most applications, we are only able to measure a finite number of data and we are typically interested in a finite number of properties. In addition, the data and properties are usually real. Therefore, in most cases there is only one option for the data space \mathcal{D} and property space \mathcal{P} : they are \mathbb{R}^{N_d} and \mathbb{R}^{N_p} where N_d, N_p are the number of data, and the number of properties respectively.

The model space \mathcal{M} is most often a function space or a finite dimensional real vector space. On a more fundamental level, we are interested in whether the space is simply a Banach space or if it possesses an inner product structure, making it a Hilbert space. Some authors have proposed solutions to inference problems in Banach spaces (e.g., Stark 2008; Al-Attar 2021), while most others have focused on the more structured Hilbert space (e.g., Backus & Gilbert 1967b; Backus 1970a; Al-Attar 2021; Pijpers & Thompson 1994; Zaroli 2016), as this simplifies the mathematics.

The property mapping \mathcal{T} is typically chosen to be a linear functional, as most inference problems focus on point evaluation, basis coefficients, or local averages, all of which are linear functionals. In this paper, we argue that a more careful consideration of these functionals can lead to improved results in inference problems, particularly in the context of SOLA/DLI-type inference problems (as discussed in Section 2.2).

A2 Choice of forward mapping G

We are now left with making the two most important decisions. Firstly, we need to decide whether G is a linear or non-linear mapping. Most often, the forward problem is non-linear, which leads to complicated inference problems. While there is some work on this front in the inference field (Snieder 1991), the problem is generally too difficult to tackle analytically or requires vast computational resources. For this reason, inference problems usually assume G to be linear and bounded (and therefore continuous when dealing with normed spaces), resulting in linear inferences.

For linear inferences, we can delve deeper into the structure of G . If \mathcal{M} is a Hilbert space, G is often defined as a vector of inner products with some known members of \mathcal{M} (commonly referred to as sensitivity kernels in seismology) (e.g. Backus 1970a). SOLA methods, for instance,

794 specifically use the L_2 inner product on the model space $L_2[\Omega]$ with Ω some spatial domain, leading
 795 to the well-known form of the forward operator seen in Equation (9).

796 More complicated linear forward mappings can be used if we consider that data frequently
 797 depend on multiple physical parameters, such as shear and compressional wave speeds, as well
 798 as density. These problems can be addressed by considering \mathcal{M} as a direct sum of Hilbert spaces,
 799 which itself forms a Hilbert space (e.g. Lau & Romanowicz 2021), and a forward mapping of the
 800 form given in Equation 34. In this paper, we argue that under such choices, the analysis provided
 801 by SOLA methods offers insights that are not readily accessible through DLI methods alone.

802 **A3 Without prior information**

803 The last, and arguably the most important decision, concerns prior information. We note that the
 804 choices of \mathcal{M} , \mathcal{D} , and G already encode some level of prior information. However, when referring
 805 to additional prior information, we assume that these choices have already been fixed. If we decide
 806 not to use any additional prior information, we would follow along the route of MOLA/SOLA
 807 methods (e.g. Backus & Gilbert 1970; Oldenburg 1981; Pijpers & Thompson 1994; Zaroli 2016).
 808 For these methods, it can be shown that we typically cannot directly infer $\mathcal{T}(\bar{m}) = \bar{p}$. Instead of
 809 obtaining the properties of interest, we must settle for approximate properties $\mathcal{R}(\bar{m})$ (see Fig. A1).
 810 Given only the data values and geometry, the goal is then to construct an approximate mapping \mathcal{R}
 811 such that:

$$\mathcal{R} = XG, \quad \text{where } \mathcal{R} : \mathcal{M} \rightarrow \mathcal{P} \text{ and } X : \mathcal{D} \rightarrow \mathcal{P}.$$

812 In essence, this involves determining the $N_d \times N_p$ elements of the X mapping. The original method
 813 of Backus and Gilbert (Backus & Gilbert 1967a, 1968b, 1967b, 1968a, 1970) proposed an approxi-
 814 mate mapping designed to obtain the highest-resolution local averages at N_p points of the unknown
 815 model. This mapping is obtained by minimising the cost functions for each point one by one (see
 816 Fig. A1):

$$\int_{\Omega} (J^{(k)} A^{(k)})^2 d\Omega, \quad \text{s.t.} \quad \int_{\Omega} A^{(k)} = 1$$

817 where $J^{(k)}$ is a weight function with increasing weight further away from the k -th point where
 818 maximum resolution is desired. In contrast, for SOLA Pijpers & Thompson (1994) constructed
 819 an approximate unimodular mapping that resembles the predefined \mathcal{T} by minimizing the cost
 820 function:

$$\text{Tr}[(\mathcal{T} - \mathcal{R})(\mathcal{T} - \mathcal{R})^*], \quad \text{subject to } \mathcal{R}(1) = 1,$$

821 where 1 represents the constant function on the left-hand side and the N_p -dimensional vector of
 822 ones on the right-hand side. This is the most generic formulism, a more specific form is given in
 823 Fig. A1. It turns out that solving the SOLA optimisation problem is computationally more efficient
 824 than solving the optimisation problem needed for the original Backus-Gilbert method (Al-Attar
 825 2021; Pijpers & Thompson 1992). This is due to the fact that the matrix to be inverted for SOLA
 826 depends only on the sensitivity kernels, while for the Backus-Gilbert method it depends on both
 827 the sensitivity kernels and the spatially dependent functions J^k , and thus needs to be inverted again
 828 for each k -th point.

829 For linear inferences on a Hilbert model space, where the forward mapping is defined via pro-
 830 jections onto sensitivity kernels, the approximate mapping \mathcal{R} is associated with resolving kernels.
 831 These resolving kernels offer valuable insights into the interpretation of the approximate prop-
 832 erties $\mathcal{R}(\bar{m})$. Even if data noise is ignored, the resolving kernels will be imperfect due to data
 833 incompleteness and trade-offs between physical parameters. The shape of these resolving kernels
 834 thus provides information about data limitations and parameter trade-offs.

835 **A4 With additional prior information**

836 If we introduce additional prior information, we have to choose between soft and hard prior
 837 information Backus (1988b). Hard priors are those where we assume that the true model must lie
 838 with 100% certainty within a subset of the model space.

839 The norm bound used in this paper is an example of a hard quadratic bound (see more here,
 840 Backus 1989). In this paper, we refer to linear inferences with hard prior information as DLI
 841 methods (Deterministic Linear Inferences) due to the deterministic nature of the prior information
 842 (Al-Attar 2021). However, in the literature, these kind of problems are also referred to as CIS

843 (Confidence Interval Sets) as the solutions are intervals in which the property is found (Backus
844 1988a).

845 Soft bounds can be imposed, for example, by introducing a soft prior via a regularisation term
846 that penalises some undesired feature of the model (for example, penalising large norms). Soft pri-
847 ors via penalty terms may be considered “softer” from the perspective that we prefer some models
848 to be penalised more than others, based on our belief that they are less likely to be true. However,
849 in practice, an optimisation process is carried out, resulting typically in a single solution. This solu-
850 tion strikes a balance between fitting the data and minimising the penalty. However, this is a single
851 solution, and the act of optimising a penalised cost function effectively collapses the model space
852 to a single point (thus solving the problem of non-uniqueness) and will reject any other model. In
853 contrast, a hard prior will immediately remove some models that are deemed unacceptable, but it
854 will usually keep many others that are deemed acceptable, without discriminating between them.
855 Therefore, a hard prior will be more inclusive and less stringent than a penalty-based soft prior.

856 Soft prior assumptions and similar regularisations are essential in inversion methods, as they
857 help address non-uniqueness, which cannot be resolved without such constraints. This is why in-
858 ference methods like DLI tend to have lower precision – their assumptions are too weak to break
859 the non-uniqueness. Essentially, these methods trade precision for accuracy, as weaker assump-
860 tions reduce the likelihood of introducing bias into the solution.

861 Another way to impose a soft bound is by making the model space a probabilistic space with a
862 measure to describe our prior knowledge. This would eliminate some sets of models that have zero
863 probability, but it will usually keep many models, giving higher probability to some compared to
864 others. Overall, we believe that the hard priors used in this paper are less stringent than penalty-
865 based soft priors, but more stringent than probabilistic soft priors.

866 **APPENDIX B: SURJECTIVITY OF G**

867 An inverse problem requires three components: model space \mathcal{M} , data space \mathcal{D} , and a forward
868 relation $G : \mathcal{M} \rightarrow \mathcal{D}$. In our case, let $\mathcal{M} = L_2(\Omega)$, a Hilbert space defined on a compact domain
869 $\Omega \subset \mathbb{R}$, and $\mathcal{D} = \mathbb{R}^{N_d}$ for some $N_d \in \mathbb{N}$. As discussed in Section 2.1.3 (Equation 9), the forward

Table 1: Comparison of different Backus-Gilbert based inference methods with noise-free data

	Original Backus-Gilbert (BG)	SOLA	Deterministic Linear Inferences (DLI)	SOLA-DLI
Solution	$\bar{p} \approx \int_{\Omega} R\bar{m}d\Omega$ where $R = \sum_i x_i K_i$ and x_i minimise $\int_{\Omega} J^2 R^2 d\Omega$ s.t. $\int_{\Omega} R d\Omega = 1$	$\bar{p} \approx \int_{\Omega} R\bar{m}d\Omega$ where $R = \sum_i x_i K_i$ and x_i minimise $\int_{\Omega} (R - T)^2 d\Omega$ s.t. $\int_{\Omega} R d\Omega = 1$	$\langle \mathcal{H}^{-1}(p - \bar{p}), p - \bar{p} \rangle$ $\leq M^2 - \ \bar{m}\ _{\mathcal{M}}^2$	$\bar{p} \in \bar{p} + [-\epsilon, +\epsilon]$ where $\epsilon = \sqrt{(M^2 - \ \bar{m}\ _{\mathcal{M}}^2) \text{diag}(\mathcal{H})}$
Prior Information	None	None	$\ \bar{m}\ \leq M$	$\ \bar{m}\ \leq M$
Interpretation of Results	Resolving Kernel	Resolving Kernel	Target Kernel	Target Kernel (+ Resolving Kernels)
Contaminant Kernels Used?	No	Yes	No	Yes
Can Produce Model/Model Proxy	Model Proxy	Model Proxy	Model	Model
References	Backus & Gilbert (1967b, 1968a, 1970, 1968b)	Oldenburg (1981); Pijpers & Thompson (1994); Masters & Gubbins (2003); Zaroli (2016, 2019)	Backus (1970a,b,c); Parker (1977); Al-Attar (2021)	This contribution

Figure A1. Comparison of different Backus-Gilbert based inference methods in the literature in the case of noise-free data. Note that the original papers use A instead of R for resolving (or averaging) kernels, but we prefer the general R as we consider a range of targets.

870 relation is defined as:

$$[G(m)]_i = \int_{\Omega} K_i(x)m(x) dx. \quad (\text{B.1})$$

871 with $x \in \Omega$. To demonstrate that G is surjective, we utilise its dual G' . The dual space \mathcal{M}' consists
872 of linear forms $m' \in \mathcal{M}'$ defined on \mathcal{M} that map elements $m \in \mathcal{M}$ to \mathbb{R} :

$$m' : \mathcal{M} \rightarrow \mathbb{R}$$

873 Since \mathcal{M} is a Hilbert space, the Riesz Representation Theorem establishes an isomorphism $\mathcal{L}_{\mathcal{M}} : \mathcal{M}' \rightarrow \mathcal{M}$. This means that for each $m \in \mathcal{M}$, there exists a unique $m' \in \mathcal{M}'$ such that

$$\mathcal{L}_{\mathcal{M}}(m') = m.$$

875 Similarly, the dual space of the data space \mathcal{D} is \mathcal{D}' with an isomorphism $\mathcal{L}_{\mathcal{D}} : \mathcal{D}' \rightarrow \mathcal{D}$. If
 876 $G : \mathcal{M} \rightarrow \mathcal{D}$, then the dual mapping is defined by

$$d'(G(m)) = (G'(d'))(m), \forall m \in \mathcal{M}, \forall d \in \mathcal{D}$$

877 Rearranging gives:

$$d'(d) = m'(m).$$

878 We can express the relationship between the spaces as:

$$m' = \mathcal{L}_{\mathcal{M}} \circ G' \circ \mathcal{L}_{\mathcal{D}}^{-1}(d).$$

879 We can define G^* , the adjoint of G , as:

$$G^* = \mathcal{L}_{\mathcal{M}} \circ G' \circ \mathcal{L}_{\mathcal{D}}^{-1}. \quad (\text{B.2})$$

880 An equivalent definition states:

$$\langle G(m), d \rangle_{\mathcal{D}} = \langle m, G^*(d) \rangle_{\mathcal{M}}, \forall d \in \mathcal{D}, m \in \mathcal{M} \quad (\text{B.3})$$

881 where $\langle \cdot, \cdot \rangle_{\mathcal{M}}$ denotes the inner product on \mathcal{M} and similarly $\langle \cdot, \cdot \rangle_{\mathcal{D}}$ is the inner product on \mathcal{D} . This
 882 implies

$$G^*(d) = \sum_i^{N_d} d_i K_i(x).$$

883 where $x \in \Omega$. We can now prove the surjectivity of G .

884 *Proof.* According to Proposition 2.1 from Al-Attar (2021), G is surjective if and only if $\ker(G') =$
 885 $\{0\}$, where

$$\ker(G') = \{d' \in \mathcal{D}' \mid G'(d') = 0\}.$$

886 Using the relation between the dual and the adjoint of G (Equation B.2), we find that:

$$G' = \mathcal{L}_{\mathcal{M}}^{-1} G^* \mathcal{L}_{\mathcal{D}}$$

887 where we have omitted the composition symbol “ \circ ”. Therefore, we have to show that:

$$\ker(\mathcal{L}_{\mathcal{M}}^{-1} G^* \mathcal{L}_{\mathcal{D}}) = \{0\}.$$

888 We will show this by assuming the contrary and showing that it leads to a contradiction. Let us

889 assume that there exists a $d' \in \mathcal{D}'$, $d' \neq 0$ such that $\mathcal{L}_{\mathcal{M}}^{-1}G^*\mathcal{L}_{\mathcal{D}}(d') = 0 \in \mathcal{M}'$. We know that $\mathcal{L}_{\mathcal{D}}$ is
 890 an isomorphism, therefore $\mathcal{L}_{\mathcal{D}}(d') \in \mathcal{D}$ and $\mathcal{L}_{\mathcal{D}}(d') \neq 0$. Applying the adjoint of G , we have:

$$G^*(\mathcal{L}_{\mathcal{D}}(d')) = \sum_i^{N_d} [\mathcal{L}_{\mathcal{D}}(d')]_i K_i(x)$$

891 However, $\{K_i\}$ are linearly independent, therefore

$$G^*(\mathcal{L}_{\mathcal{D}}(d')) = \sum_i^{N_d} [\mathcal{L}_{\mathcal{D}}(d')]_i K_i(x) = 0 \in \mathcal{M} \text{ iff } \mathcal{L}_{\mathcal{D}}(d') = 0$$

892 which we already know is not the case. This means that $G^*(\mathcal{L}_{\mathcal{D}}(d')) \neq 0 \in \mathcal{M}$. Since $\mathcal{L}_{\mathcal{M}}^{-1}$ is
 893 bijective, the non-zero element $G^*(\mathcal{L}_{\mathcal{D}}(d'))$ gets mapped onto a non-zero element of \mathcal{M}' , which
 894 contradicts the initial assumption. \square

895 As a final note, we want to emphasise that the approximate nature of the theory does not imply
 896 that G is not surjective (as we have proven above).

897 **APPENDIX C: X FROM SOLA**

898 For SOLA inferences, in the absence of unimodularity conditions, we want to solve:

$$\operatorname{argmin}_{x_i^{(k)}} \left[\int_{\Omega} (T^{(k)} - \sum_i^{N_d} x_i^{(k)} K_i)^2 d\Omega \right] \quad (\text{C.1})$$

899 Mathematically, this is a multi-objective minimisation problem, because we want to find $x_i^{(k)}$ that
 900 minimise concomitantly all squared differences between the targets and their corresponding aver-
 901 aging kernels. Since we give the same importance to each target-resolving kernel error we want to
 902 minimise, we can use the classic Pareto method. In other words, we try to minimise:

$$\operatorname{argmin}_{x_i^{(k)}} \left[\sum_k^{N_p} \int_{\Omega} (T^{(k)} - \sum_i^{N_d} x_i^{(k)} K_i)^2 d\Omega \right] \quad (\text{C.2})$$

903 In practice, the minimisation problem for each property can be solved independently for all other
 904 properties (mathematically equivalent to Equation C.2). This leads to an embarrassingly parallel
 905 algorithm (Zaroli et al. 2017).

906 Using matrix calculus, the solution can readily be found. We first take the gradient of Equation

907 C.2 and set it to zero:

$$\frac{\partial}{\partial x_l^{(q)}} \sum_k^{N_p} \left[\int_{\Omega} (T^{(k)} - \sum_i^{N_d} x_i^{(k)} K_i)^2 d\Omega \right] = 0. \quad (\text{C.3})$$

908 Because

$$\frac{\partial}{\partial x_l^{(q)}} \left(T^{(k)} - \sum_i^{N_d} x_i^{(k)} K_i \right)^2 = -2 \left(T^{(k)} - \sum_i^{N_d} x_i^{(k)} K_i \right) \left(\sum_j^{N_m} \frac{\partial x_j^{(k)}}{\partial x_l^{(q)}} K_j \right)$$

909 Equation C.3 becomes:

$$-2 \sum_k^{N_p} \int_{\Omega} \left(T^{(k)} - \sum_i^{N_d} x_i^{(k)} K_i \right) \left(\sum_j^{N_m} \frac{\partial x_j^{(k)}}{\partial x_l^{(q)}} K_j \right) d\Omega = 0 \quad (\text{C.4})$$

910 It is obviously that:

$$\frac{\partial x_j^{(k)}}{\partial x_l^{(q)}} = \delta_{lj} \delta_{qk},$$

911 which can be substituted in Equation C.4 to obtain:

$$\int_{\Omega} \left(T^{(q)} - \sum_i^{N_d} x_i^{(q)} K_i \right) K_l d\Omega = 0. \quad (\text{C.5})$$

912 Separating the integral in Equation C.5, we now get:

$$\sum_i^{N_d} x_i^{(q)} \int_{\Omega} K_i K_l d\Omega = \int_{\Omega} T^{(q)} K_l d\Omega.$$

913 This can be written in matrix form as:

$$X\Lambda = \Gamma,$$

914 where

$$\begin{aligned} \Lambda_{il} &= \int_{\Omega} K_i K_l d\Omega \\ \Gamma_{ql} &= \int_{\Omega} T^{(q)} K_l d\Omega \\ X_{qi} &= x_i^{(q)}. \end{aligned}$$

915 This finally gives us:

$$X = \Gamma\Lambda^{-1} \quad (\text{C.6})$$

916 which is equivalent to the Equations 18, 19, and 20.

917 **APPENDIX D: ELEMENTS NEEDED FOR THE DERIVATION OF THE SOLA-DLI**
 918 **SOLUTION**

919 In this appendix we derive some further equations and equalities related to the material presented
 920 in Section 2.1.

921 **D1 Data-model relationships**

922 Given a model $m = (m^1, m^2, \dots)$, the relationship between the model and data is defined by:

$$d_i = [G(m)]_i = \sum_j^{N_m} \langle K_i^j, m^j \rangle_{\mathcal{M}_j}. \quad (\text{D.1})$$

923 It is useful to define:

$$G^j(m) = \langle K_i^j, m^j \rangle_{\mathcal{M}_j} \quad (\text{D.2})$$

$$G = \sum_j^{N_m} G^j. \quad (\text{D.3})$$

924 The adjoint of G is defined in Equation B.3 and repeated for convenience:

$$\langle G(m), d' \rangle_{\mathcal{D}} = \langle m, G^*(d') \rangle_{\mathcal{M}} \quad (\text{D.4})$$

925 for all $m \in \mathcal{M}$ and $d' \in \mathcal{D}$. We expand the LHS:

$$\sum_i^{N_d} \sum_j^{N_m} \langle K_i^j, m^j \rangle_{\mathcal{M}_j} d'_i = \langle m, G^*(d') \rangle_{\mathcal{M}} \quad (\text{D.5})$$

926 For the RHS, we use the formula for the inner product in the direct sum space \mathcal{M} :

$$\langle a, b \rangle_{\mathcal{M}} = \sum_j^{N_m} \langle a^j, b^j \rangle_{\mathcal{M}_j} \quad (\text{D.6})$$

927 where a, b are some members of \mathcal{M} . Therefore, we write

$$\sum_i^{N_d} \sum_j^{N_m} \langle K_i^j, m^j \rangle_{\mathcal{M}_j} d'_i = \sum_j^{N_m} \langle m^j, G^{j*}(d') \rangle_{\mathcal{M}_j} \quad (\text{D.7})$$

928 Taking the sum over i inside, we can also write:

$$\sum_j^{N_m} \left\langle \sum_i^{N_d} d'_i K_i^j, m^j \right\rangle_{\mathcal{M}_j} = \sum_j^{N_m} \langle m^j, G^{j*}(d') \rangle_{\mathcal{M}_j} \quad (\text{D.8})$$

929 and we identify:

$$G^{j*}(d') = \sum_i^{N_d} d'_i K_i^j \quad (\text{D.9})$$

$$G^* = (G^{1*}, G^{2*}, \dots) \quad (\text{D.10})$$

930 G^* maps elements from the data space to elements (tuples) in the model space. A similar approach
 931 shows that the adjoint of the property mapping \mathcal{T} is given by:

$$\mathcal{T}^{j*}(p) = \sum_k^{N_p} p^{(k)} T^{j,(k)} \quad (\text{D.11})$$

$$\mathcal{T}^* = (\mathcal{T}^{1*}, \mathcal{T}^{2*}, \dots) \quad (\text{D.12})$$

932 D2 H matrix

933 The \mathcal{H} matrix introduced in Section 2.1 quantifies the difference between the target and resolving
 934 kernels. It is defined by Al-Attar (2021, see Equation 2.84) as:

$$\mathcal{H} = HH^* \quad (\text{D.13})$$

$$H = \mathcal{T} - \mathcal{R} \quad (\text{D.14})$$

935 where \mathcal{R} is the “approximate mapping”, given by:

$$\mathcal{R} = \mathcal{T}G^*(GG^*)^{-1}G \quad (\text{D.15})$$

936 This mapping takes any model $m \in \mathcal{M}$ into the data space $d \in \mathcal{D}$, then finds the least norm
 937 solution to $G(m) = d$ and maps this least norm solution into the property space. When applied
 938 to one of the possible model solutions $U_M \cap S$ (see Fig. 1b), it gives the property of the model
 939 solution that has the smallest norm. Combining (D.13), (D.14), and (D.15) we obtain:

$$\mathcal{H} = (\mathcal{T} - \mathcal{R})(\mathcal{T} - \mathcal{R})^* \quad (\text{D.16})$$

$$\mathcal{H} = \mathcal{T}\mathcal{T}^* - \mathcal{T}G^*(GG^*)^{-1}G\mathcal{T}^* \quad (\text{D.17})$$

940 Let us denote

$$\Lambda := GG^*. \quad (\text{D.18})$$

941 Using a simple application of Equation (D.1) and (D.10), we can then easily obtain:

$$\Lambda_{iq} = \sum_j^{N_m} \langle K_i^j, K_q^j \rangle_{\mathcal{M}_j} \quad (\text{D.19})$$

942 Similarly, we denote:

$$\chi := \mathcal{T}\mathcal{T}^* \quad (\text{D.20})$$

$$\chi_{k,l} = \sum_j^{N_m} \langle T^{j,(k)}, T^{j,(l)} \rangle_{\mathcal{M}_j} \quad (\text{D.21})$$

943 and

$$\Gamma := \mathcal{T}G^* \quad (\text{D.22})$$

$$\Gamma_{ki} = \sum_j^{N_m} \langle T^{j,(k)}, K_i^j \rangle_{\mathcal{M}_j} \quad (\text{D.23})$$

944 Using the definitions of Λ, χ, Γ we can write (D.17) as:

$$\mathcal{H} = \chi - \Gamma\Lambda^{-1}\Gamma^T. \quad (\text{D.24})$$

945 Figure A2 provides a visualisation of the ellipse in the property space as determined by \mathcal{H} when
946 only two properties are considered.

947 **D3 Error Bounds**

948 The error bounds defined in Equations 23 and 24 are derived from the property bounds defined by
949 Al-Attar (2021, see Equation 2.84) as:

$$\langle \mathcal{H}^{-1}(p - \tilde{p}), p - \tilde{p} \rangle_{\mathcal{P}} \leq M^2 - \|\tilde{m}\|_{\mathcal{M}}^2 \quad (\text{D.25})$$

950 Equation (D.25) describes a hyperellipsoid centered on \tilde{p} with major axes given by the eigenvalues
951 of \mathcal{H}^{-1} scaled by $\sqrt{M^2 - \|\tilde{m}\|_{\mathcal{M}}^2}$. If the matrix \mathcal{H} is diagonal, then the inverse is trivial to find
952 and the hyperellipsoid has its major axes aligned with the coordinate axes of the property space.
953 In all other cases, the hyperellipsoid will have some arbitrary orientation and \mathcal{H} will be difficult to
954 invert numerically.

955 To avoid numerical complications, we use here a different, more relaxed approximation for the

956 error bounds given in the form:

$$\|p - \tilde{p}\|_{\mathcal{P}}^2 \leq (M^2 - \|\tilde{m}\|_{\mathcal{M}}^2) \text{diag}(\mathcal{H}) \quad (\text{D.26})$$

957 where $\text{diag}(\mathcal{H})$ is the diagonal of \mathcal{H} . We can also write this in component form:

$$\|p^{(k)} - \tilde{p}^{(k)}\|_{\mathcal{P}}^2 \leq (M^2 - \|\tilde{m}\|_{\mathcal{M}}^2) \mathcal{H}_{kk} \quad (\text{D.27})$$

958 Inequality (D.27) describes a hyperparallelepiped that contains the error bounds of (D.25) with
 959 sides parallel to the coordinate axes of \mathcal{P} (see Fig. A2). As this approximation does not require
 960 the inversion of the \mathcal{H} matrix, it is computationally advantageous. Visually, the hyperellipsoid
 961 fits “perfectly” inside the hyperparallelepiped (Fig. A2), but the error bounds of the hyperpar-
 962 allelepiped are easier to visualise in a static plot (see for example first column of Fig. 7). The
 963 hyperellipsoid encodes the correlations between the error bounds of the various components of the
 964 property vector (such as the correlation between the error bounds of two different local averages).
 965 Plotting the bounds for each component of the property vector simultaneously would therefore be
 966 very difficult, since the error bounds of each property component would depend on the values of
 967 the bounds on all other property components. The hyperparallelepiped ignores these correlations,
 968 simplifying thus the plotting. However, it overestimates the property bounds, which will likely
 969 make it more difficult to interpret the property values.

970 To show how (D.27) arises from (D.25), we need to prove the following:

Given that

$$x^T A^{-1} x \leq b \quad (\text{D.28})$$

Show that

$$x_k^2 \leq b A_{kk} \quad (\text{D.29})$$

971 where $x = \tilde{p} - \epsilon$, $A = \mathcal{H}$, and $b = M^2 - \|\tilde{m}\|_{\mathcal{M}}^2$. To prove this, we start by finding the maxi-
 972 mum extent of the hyperellipsoid (D.28) along the k^{th} coordinate axis, which can be described

973 mathematically as:

$$\text{Find } \max(c^T x) \quad (\text{D.30})$$

$$\text{Given that } x^T A^{-1} x \leq b. \quad (\text{D.31})$$

974 where c^T will be chosen later to be a vector with all entries 0 except the k^{th} one. We shall use
 975 the Lagrangian approach to solve this problem. We introduce the slack constant s and use it to
 976 transform the inequality D.31 into an equality (slack constraint):

$$x^T A^{-1} x - b + s^2 = 0 \quad (\text{D.32})$$

977 Let λ be a Lagrange multiplier. The problem then becomes finding the extremum points of the
 978 Lagrangian:

$$f(x, \lambda) = c^T x + \lambda(b - x^T A^{-1} x - s^2). \quad (\text{D.33})$$

979 Differentiating f with respect to x and setting the result to zero leads to:

$$c - 2\lambda A^{-1} x = 0. \quad (\text{D.34})$$

980 Notice that $\lambda = 0$ leads to $c = 0$, which is a contradiction. Therefore we must have $\lambda \neq 0$ and
 981 $s^2 = 0$, which means that our constraint is active. Assuming A^{-1} to be invertible, we obtain:

$$x = \frac{Ac}{2\lambda}. \quad (\text{D.35})$$

982 We next differentiate f with respect to λ (using $s^2 = 0$ since we have shown the constraint to be
 983 active) to obtain the second Lagrange equation. Setting the result equal to zero leads to:

$$b - x^T A^{-1} x = 0. \quad (\text{D.36})$$

984 Substituting (D.35) into (D.36) and rearranging for b , we obtain:

$$b = \left(\frac{Ac}{2\lambda} \right)^T A^{-1} \frac{Ac}{2\lambda}. \quad (\text{D.37})$$

985 Since A is symmetric this leads to:

$$\lambda^2 = \frac{c^T A c}{4b}. \quad (\text{D.38})$$

986 Assuming that A is positive definite (its eigenvalues give the lengths of the hyperellipsoids' major

axes), we must have

$$\lambda = \frac{\sqrt{c^T A c}}{2\sqrt{b}}. \quad (\text{D.39})$$

Finally, using (D.38) and (D.35) the optimal vector solution x can be expressed for any vector c as:

$$x = \frac{A c}{2\lambda} = \frac{A c}{\frac{\sqrt{c^T A c}}{\sqrt{b}}} = \frac{\sqrt{b} A c}{\sqrt{c^T A c}}, \quad (\text{D.40})$$

and the maximal value of $c^T x$ is thus:

$$\sqrt{b c^T A c}. \quad (\text{D.41})$$

Now, we consider a fixed index k between 1 and N , and we define c to be the following vector:

$$c := (\delta_{ik})_{1 \leq i \leq N}, \quad (\text{D.42})$$

where δ_{ik} is 1 if $i = k$, and 0 if $i \neq k$. Substituting this for c in (D.41), we obtain:

$$\max(x_k) = \sqrt{b A_{kk}} \quad (\text{D.43})$$

or equivalently:

$$x_k \leq \sqrt{b A_{kk}} \quad (\text{D.44})$$

If instead we choose $c = -\delta_{ik}$, then we have:

$$x_k \geq -\sqrt{b A_{kk}} \quad (\text{D.45})$$

These two inequalities can be summarised in the final answer:

$$(x_k)^2 \leq b A_{kk} \quad (\text{D.46})$$

REFERENCES

- Al-Attar, D., 2021. Linear inference problems with deterministic constraints, *arXiv preprint arXiv:2104.12256*.
- Amiri, S., Maggi, A., Tatar, M., Zigone, D., & Zaroli, C., 2023. Rayleigh wave group velocities in north-west iran: Sola backus-gilbert vs. fast marching tomographic methods, *Seismica*, **2**(2).
- Backus, G., 1970a. Inference from inadequate and inaccurate data, i, *Proceedings of the National Academy of Sciences*, **65**(1), 1–7.

Table A1. Table summarising the main mathematical symbols used in the manuscript. Elements are grouped on columns and rows depending on the relationships between them. For example, \bar{m} is part of the model space \mathcal{M} and is related to \bar{d} through G , which is determined by K . Similarly, \bar{p} is related to \bar{m} through \mathcal{R} and to \tilde{m} through \mathcal{T} .

\mathcal{M}	\mathcal{D}	\mathcal{P}		
Model space	Data space	Property space	Mapping	Kernels
\bar{m} : TRUE model	\bar{d} : TRUE data		G : Forward mapping	K : Sensitivity kernels
\bar{m} : TRUE model		\bar{p} : TRUE property	\mathcal{T} : Property mapping	T : Target kernels
\bar{m} : TRUE model		\tilde{p} : Aproximate property	\mathcal{R} : Approximate mapping	R : Resolving kernels
\tilde{m} : Least norm model		\tilde{p} : Aproximate property	\mathcal{T} : Property mapping	T : Target kernels
		ϵ : Property error	\mathcal{H} : Hyperellipsoid matrix	
j : Physical parameter index	i : Data index	k : Property index		
N_m : Number of physical parameters	N_d : number of data			N_p : Number of properties

- 1003 Backus, G., 1970b. Inference from inadequate and inaccurate data, iii, *Proceedings of the National*
1004 *Academy of Sciences*, **67**(1), 282–289.
- 1005 Backus, G., 1970c. Inference from inadequate and inaccurate data, ii; $\sup_i \sup_j$, *Proceedings of the*
1006 *National Academy of Sciences*, **65**(2), 281–287.
- 1007 Backus, G. & Gilbert, F., 1968a. The resolving power of gross earth data, *Geophysical Journal Interna-*
1008 *tional*, **16**(2), 169–205.
- 1009 Backus, G. & Gilbert, F., 1968b. The resolving power of gross earth data, *Geophysical Journal Interna-*
1010 *tional*, **16**(2), 169–205.
- 1011 Backus, G. & Gilbert, F., 1970. Uniqueness in the inversion of inaccurate gross earth data, *Philosophical*
1012 *Transactions of the Royal Society of London. Series A, Mathematical and Physical Sciences*, **266**(1173),
1013 123–192.
- 1014 Backus, G. E., 1988a. Bayesian inference in geomagnetism, *Geophysical Journal International*, **92**(1),
1015 125–142.
- 1016 Backus, G. E., 1988b. Comparing hard and soft prior bounds in geophysical inverse problems, *Geophysical*
1017 *Journal International*, **94**(2), 249–261.
- 1018 Backus, G. E., 1989. Confidence set inference with a prior quadratic bound, *Geophysical Journal Inter-*

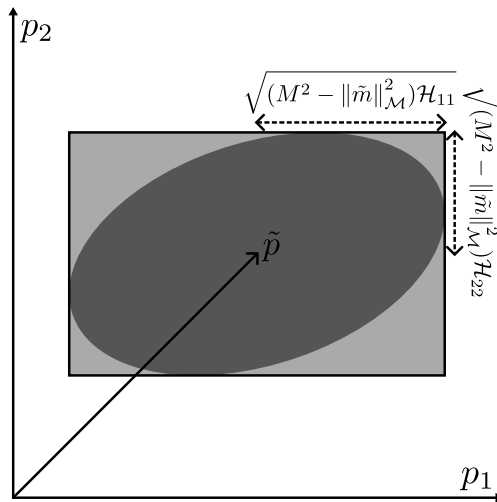


Figure A2. Illustration of the relationship between the hyperellipsoid defined in Equation D.25 and the hyperparallelepiped defined in Equation D.27 for the case when the property space is two-dimensional. p_1 and p_2 could represent, for example, two local averages at two different spatial locations. The dark shaded ellipse contains all the possible combinations of these two properties given by the tighter inequality of Equation D.25. The lighter gray shaded rectangle contains all the possible combinations of these two properties under the simplified inequality in Equation D.27.

- 1019 *national*, **97**(1), 119–150.
- 1020 Backus, G. E. & Gilbert, J., 1967a. Numerical applications of a formalism for geophysical inverse prob-
1021 lems, *Geophysical Journal International*, **13**(1-3), 247–276.
- 1022 Backus, G. E. & Gilbert, J. F., 1967b. Numerical applications of a formalism for geophysical inverse
1023 problems, *Geophysical Journal International*, **13**(1-3), 247–276.
- 1024 Fichtner, A. & Trampert, J., 2011. Resolution analysis in full waveform inversion, *Geophysical Journal
1025 International*, **187**(3), 1604–1624.
- 1026 Freissler, R., Schuberth, B. S. A., & Zaroli, C., 2024. A concept for the global assessment of tomographic
1027 resolution and uncertainty, *Geophysical Journal International*, p. gga178.
- 1028 Harris, C. R., Millman, K. J., van der Walt, S. J., Gommers, R., Virtanen, P., Cournapeau, D., Wieser, E.,
1029 Taylor, J., Berg, S., Smith, N. J., Kern, R., Picus, M., Hoyer, S., van Kerkwijk, M. H., Brett, M., Haldane,
1030 A., del Río, J. F., Wiebe, M., Peterson, P., Gérard-Marchant, P., Sheppard, K., Reddy, T., Weckesser, W.,
1031 Abbasi, H., Gohlke, C., & Oliphant, T. E., 2020. Array programming with NumPy, *Nature*, **585**(7825),
1032 357–362.
- 1033 Hunter, J. D., 2007. Matplotlib: A 2d graphics environment, *Computing in Science & Engineering*, **9**(3),
1034 90–95.
- 1035 Koelemeijer, P., Ritsema, J., Deuss, A., & Van Heijst, H.-J., 2016. SP12RTS: a degree-12 model of shear-
1036 and compressional-wave velocity for Earth’s mantle, *Geophys. J. Int.*, **204**(2), 1024–1039.

- 1037 Latallerie, F., Zaroli, C., Lambotte, S., & Maggi, A., 2022. Analysis of tomographic models using res-
1038 olution and uncertainties: a surface wave example from the pacific, *Geophysical Journal International*,
1039 **230**(2), 893–907.
- 1040 Latallerie, F., Zaroli, C., Lambotte, S., Maggi, A., Walker, A., & Koelemeijer, P., 2024. Surface-wave
1041 tomography with 3d resolution and uncertainty, *Seismica*.
- 1042 Lau, H. C. & Romanowicz, B., 2021. Constraining jumps in density and elastic properties at the 660
1043 km discontinuity using normal mode data via the backus-gilbert method, *Geophysical Research Letters*,
1044 **48**(9), e2020GL092217.
- 1045 Mag, A., Zaroli, C., & Koelemeijer, P., 2024. Adrian-Mag/SOLA_DLI: SOLA-DLI.
- 1046 Masters, G. & Gubbins, D., 2003. On the resolution of density within the Earth, *Phys. Earth Planet. Inter.* ,
1047 **140**(1-3), 159–167.
- 1048 Nolet, G., 2008. A breviary of seismic tomography, *A Breviary of Seismic Tomography*, by Guust Nolet,
1049 Cambridge, UK: Cambridge University Press, 2008.
- 1050 Oldenburg, D., 1981. A comprehensive solution to the linear deconvolution problem, *Geophysical Journal*
1051 *International*, **65**(2), 331–357.
- 1052 Parker, R. L., 1977. Linear inference and underparameterized models, *Reviews of Geophysics*, **15**(4),
1053 446–456.
- 1054 Pijpers, F. & Thompson, M., 1992. Faster formulations of the optimally localized averages method for
1055 helioseismic inversions, *Astronomy and Astrophysics (ISSN 0004-6361)*, vol. 262, no. 2, p. L33-L36.,
1056 **262**, L33–L36.
- 1057 Pijpers, F. & Thompson, M., 1994. The sola method for helioseismic inversion, *Astronomy and Astro-*
1058 *physics (ISSN 0004-6361)*, vol. 281, no. 1, p. 231-240, **281**, 231–240.
- 1059 Rawlinson, N., Pozgay, S., & Fishwick, S., 2010. Seismic tomography: a window into deep earth, *Physics*
1060 *of the Earth and Planetary Interiors*, **178**(3-4), 101–135.
- 1061 Restelli, F., Zaroli, C., & Koelemeijer, P., 2024. Robust estimates of the ratio between s- and p-wave ve-
1062 locity anomalies in the earth’s mantle using normal modes, *Physics of the Earth and Planetary Interiors*,
1063 **347**, 107135.
- 1064 Ritsema, J. & Lekić, V., 2020. Heterogeneity of seismic wave velocity in earth’s mantle, *Annual Review*
1065 *of Earth and Planetary Sciences*, **48**, 377–401.
- 1066 Snieder, R., 1991. An extension of backus-gilbert theory to nonlinear inverse problems, *Inverse Problems*,
1067 **7**(3), 409.
- 1068 Stark, P. B., 2008. Generalizing resolution, *Inverse Problems*, **24**(3), 034014.
- 1069 Stark, P. B. & Hengartner, N. W., 1993. Reproducing earth’s kernel: Uncertainty of the shape of the core-
1070 mantle boundary from pkp and pcp travel times, *Journal of Geophysical Research: Solid Earth*, **98**(B2),
1071 1957–1971.

- 1072 Tarantola, A., 1987. *Inverse problem theory*, Elsevier, Amsterdam.
- 1073 Trampert, J. & Snieder, R., 1996. Model estimations biased by truncated expansions: possible artifacts in
1074 seismic tomography, *Science*, **271**(5253), 1257–1260.
- 1075 Valentine, A. P. & Sambridge, M., 2023. Emerging directions in geophysical inversion, *Applications of*
1076 *Data Assimilation and Inverse Problems in the Earth Sciences*, **5**(9).
- 1077 Virtanen, P., Gommers, R., Oliphant, T. E., Haberland, M., Reddy, T., Cournapeau, D., Burovski, E.,
1078 Peterson, P., Weckesser, W., Bright, J., van der Walt, S. J., Brett, M., Wilson, J., Millman, K. J., Mayorov,
1079 N., Nelson, A. R. J., Jones, E., Kern, R., Larson, E., Carey, C. J., Polat, İ., Feng, Y., Moore, E. W.,
1080 VanderPlas, J., Laxalde, D., Perktold, J., Cimrman, R., Henriksen, I., Quintero, E. A., Harris, C. R.,
1081 Archibald, A. M., Ribeiro, A. H., Pedregosa, F., van Mulbregt, P., & SciPy 1.0 Contributors, 2020. SciPy
1082 1.0: Fundamental Algorithms for Scientific Computing in Python, *Nature Methods*, **17**, 261–272.
- 1083 Woodhouse, J. H. & Dahlen, F. A., 1978. The effect of a general aspherical perturbation on the free
1084 oscillations of the earth, *Geophysical Journal International*, **53**(2), 335–354.
- 1085 Zaroли, C., 2016. Global seismic tomography using Backus–Gilbert inversion, *Geophysical Journal Inter-*
1086 *national*, **207**(2), 876–888.
- 1087 Zaroли, C., 2019. Seismic tomography using parameter-free backus–gilbert inversion, *Geophysical Journal*
1088 *International*, **218**(1), 619–630.
- 1089 Zaroли, C., Koelemeijer, P., & Lambotte, S., 2017. Toward seeing the earth’s interior through unbiased
1090 tomographic lenses, *Geophysical Research Letters*, **44**(22), 11–399.